Two-qubit gate in neutral atoms using transitionless quantum driving

Archismita Dalal [*] and Barry C. Sanders [†]
Institute for Quantum Science and Technology, University of Calgary, Calgary, Alberta, Canada T2N 1N4

(Received 6 July 2022; accepted 20 December 2022; published 9 January 2023)

A neutral-atom system serves as a promising platform for realizing gate-based quantum computing because of its capability to trap and control several atomic qubits in different geometries and the ability to perform strong, long-range interactions between qubits; however, the two-qubit entangling gate fidelity lags behind competing platforms such as superconducting systems and trapped ions. The aim of our work is to design a fast, robust, high-fidelity controlled-Z (CZ) gate, based on the Rydberg-blockade mechanism, for neutral atoms. We propose a gate procedure that relies on simultaneous and transitionless quantum driving of a pair of atoms using broadband lasers. By simulating a system of two interacting cesium atoms, including spontaneous emission from excited levels and parameter fluctuations, we yield a Rydberg-blockade CZ gate with fidelity 0.9985 over an operation time of 0.12 μs. Our gate procedure delivers CZ gates that are superior than the state-of-the-art experimental CZ gate and the simulated CZ gates based on adiabatic driving of atoms. Our results show that our gate procedure carries significant potential for achieving scalable quantum computing using neutral atoms.

DOI: 10.1103/PhysRevA.107.012605

I. INTRODUCTION

The aim of this work is to develop a procedure for implementing a high-performance entangling gate on a pair of neutral alkali atoms trapped in an optical lattice. Our work is important because neutral-atom quantum computing is one of the most promising architecture of quantum computing [1–5]. Popular two-qubit gates for atomic qubits utilize the strong dipole-dipole interaction between Rydberg-excited atoms [6], and such "Rydberg-blockade" gates have been explored in both theory [1,5,7,8] and experiments [9–11]. Gate performance is typically quantified in terms of the Bell-state preparation fidelity (F_g), which is indicative of the quantum-algorithmic performance, and gate-implementation time (T_g), which is required to be short for avoiding decoherence and yielding high clock rates [12]. We propose a procedure for designing time-dependent functions for laser pulses driving the pair of atoms simultaneously and thereby effecting the controlled-Z (CZ) gate. In the presence of spontaneous emission from excited levels of these atoms and major technical imperfections, our procedure results in a simulated Rydberg-blockade CZ gate with higher F_g and lower T_g than state-of-the-art CZ implementations [9,11].

The promise of neutral atoms for quantum computing materialized with the advent of Rydberg-blockade gate procedures [7] and the capability to trap multiple atoms almost deterministically using optical tweezers [13,14]. The potential of this platform stems from its inherent ability to control several qubits coherently in different geometries [15,16] and to facilitate long-range interactions between qubits. Quantum information is encoded either in the long-lived hyperfine levels of the ground state ("ground-ground" [4]) or in a superposition of ground and highly excited Rydberg states ("ground-Rydberg" [4]), where all qubits are identical and can be well isolated from their environment. Experiments have already achieved $F_g > 0.99$ ("two nines") for single-qubit gates [15,16], accompanied by high efficiencies for state initialization and detection [10]. In addition to performing universal computation, this platform has the ability to simulate quantum dynamics [17,18]. Industrial efforts towards achieving commercial quantum computing is rapidly intensifying [19–22].

Although neutral atoms deliver a versatile platform for quantum technologies, scalable quantum computing using ground-ground encoding suffers from low F_g (below two nines) for two-qubit gates [9,11]. In contrast, ground-Rydberg encoding delivers two-nine fidelity but suffers from low coherence [10]. Neutral-atom two-qubit gate fidelities are far behind competing platforms such as superconducting systems [23,24] and ion traps [25], and they do not even reach the required thresholds for error-correcting codes [1]. One promising method for delivering "three-nine" two-qubit gate fidelity ($F_g > 0.999$) is to employ adiabatic pulses with optimal parameters [26], but such gates are fundamentally slow. Here we propose a best-of-both-worlds approach using shortcut to adiabaticity [27] for designing pulses that yield fast, robust, and high-fidelity CZ gates for atomic qubits.

We adapt the transitionless quantum driving (TQD) technique [28], commonly used for achieving shortcut to adiabaticity, to design time-dependent laser pulse sequences that yield a high-performing Rydberg-blockade gate. We consider both one-photon and two-photon driving of atoms between their ground and Rydberg levels. Single-photon driving is challenging because it requires an ultraviolet laser, which is extremely sensitive to Doppler broadening [29]. Two-photon driving circumvents these problems but requires stronger driving and yields lower F_g for adiabatic CZ gates [26]. Our method for pulse design applies both one- and two-photon cases, and combines our modified TQD technique with a

[*] archismita.dalal1@ucalgary.ca
[†] sandersb@ucalgary.ca

pulse-concatenation technique [9] to yield fast, high-fidelity two-qubit gates.

We numerically integrate the quantum master equation to simulate the Rydberg-blockade CZ gate on cesium (Cs) atoms including spontaneous emission and major technical imperfections. Our analysis predicts $F_g \approx 0.998$ over $T_g = 0.12$ μs for one-photon driving, whereas, for two-photon driving, we predict $F_g \approx 0.975$ over $T_g = 0.24$ μs. Our proposed gates outperform the recent experimental CZ gate on Cs atoms, for which $F_g \approx 0.955$ over $T_g = 0.8$ μs [11]. Our procedure delivers gates that are at least twice as fast as the adiabatic CZ gates [26], while keeping F_g and maximum laser intensities almost equal. Moreover, to achieve a noiseless (closed-system) fidelity of 0.99, laser intensity required by the adiabatic CZ gate increases five times faster than our CZ gate for decreasing T_g. Thus, our gate procedure is potentially superior to existing alternatives and paves the way for scalable neutral-atom quantum computing.

Our paper is organized as follows. Our background in Sec. II describes CZ-gate implementation on atomic qubits, followed by proposals for adiabatic CZ gates and techniques to characterise these gates in simulations. Additionally, in Sec. II we elaborate on pertinent background for TQD. We then explain our approach in Sec. III for computing time-dependent Rabi frequency and detuning functions for laser pulses, which, when applied to a pair of Cs atoms, yield fast, high-fidelity CZ gates. In Sec. IV we derive expressions for these pulse functions and present numerical results for performances of our gates compared with those obtained by the adiabatic procedure [26]. Then we analyze our results and their implications in Sec. V and conclude in Sec. VI.

II. BACKGROUND

In this section we explain key concepts and methods necessary for designing and characterizing a two-qubit gate in neutral atoms. We begin by elaborating the pertinent background on implementing, both in experiment (Sec. II A) and in simulation (Sec. II B), CZ gates on atomic qubits using the Rydberg-blockade phenomena. Then we discuss numerical techniques for simulating such gates in the presence of spontaneous emission and parameter fluctuations (Sec. II C). Finally, we explain transitionless quantum driving and its application to quantum control (Sec. II D).

A. Implementation of CZ gates

Here we describe state-of-the-art CZ implementations on ground-ground qubits of alkali atoms. Our focus are CZ gates that are effected by the Rydberg-blockade interaction and are thus native to Rydberg atoms, which means this gate is implemented in the system in a natural way and is universal. We begin by elaborating on the Rydberg-blockade CZ gate and the "standard procedure" for realizing this gate. Then we explain the gate procedure used for achieving state-of-the-art CZ gates on alkali atoms. Finally, we summarize the experimental implementation on Cs atoms and state the typical magnitudes of experimental parameters, which will be used in our numerical simulation.

Among different techniques for constructing two-qubit gates [5,30], Rydberg-blockade gates are the most popular because their fidelities are insensitive to the exact magnitude of the dipole coupling strength and are less susceptible to external motional degrees of freedom [7]. The dipole-dipole interaction between two Rydberg atoms, which is quantified by the blockade shift B [31], comes into effect only for an initial two-qubit state $|11\rangle$ and shifts its phase when this interaction is stronger than the driving lasers. This "Rydberg-blockade condition" leads to a negligible excitation of the two-atom state $|\mathrm{rr}\rangle$ throughout the gate implementation. The strong Rydberg-Rydberg interaction yields a CZ gate, up to some single-qubit phase [9,32], which is robust against the variation in B and consequently in the interatomic separation.

The standard procedure for implementing a fast Rydberg-blockade gate employs a sequential driving of the two atoms [7]. The procedure commences with preparing two atoms in a superposition of the two-qubit computational basis states $\{|00\rangle, |01\rangle, |10\rangle, |11\rangle\}$, where one atom is treated as control and the other as target. The transition between $|1\rangle$ and $|\mathrm{r}\rangle$ of each atom is effected by individual addressing with on-resonant narrow-band optical pulses. The procedure involves the following sequence: π pulse on control atom, followed by a 2π pulse on target atom and finally another π pulse on control atom. This sequence, in the ideal case, yields

$$\mathrm{CZ} := \mathrm{diag}(1, 1, 1, -1), \tag{1}$$

up to a global phase π. The most recent implementation of the CZ gate on Cs atoms using this procedure yields $F_g = 0.89$ over $T_g = 1.12$ μs [32].

As opposed to this standard procedure, the state-of-the-art procedure for implementing the CZ gate is based on simultaneous excitation of both atoms [9]. This procedure is developed by identifying sectors, generated by block-diagonalizing the Hamiltonian matrix, in the unitary dynamics of the system corresponding to the four computational basis states. The $|1\rangle \leftrightarrow |\mathrm{r}\rangle$ transition of both atoms is driven through a two-photon process of global off-resonant narrow-band optical pulses. By choosing appropriate pulse parameters, a 2π pulse effects a full Rabi cycle for $|11\rangle$, but partial cycles for $|01\rangle$ and $|10\rangle$. A sequence of two such identical 2π pulses, with an appropriate relative phase shift of ϕ_R, yields a controlled-phase gate

$$\mathrm{CZ}_\phi := \mathrm{diag}(1, e^{\mathrm{i}\phi}, e^{\mathrm{i}\phi}, e^{\mathrm{i}(2\phi+\pi)}), \tag{2}$$

which is equal to the standard CZ gate (1) up to a single-qubit phase ϕ. Based on this procedure, recent experiments yield $F_g \geqslant 0.974$ for rubidium atoms [9] and $F_g \sim 0.955$ for Cs atoms [11].

In the state-of-the-art experiment [11], which we elaborate here in detail, cold ^{133}Cs atoms at temperature $T_a = 5$ μK are trapped in a 7×7 site optical lattice with period $d = 3$ μm. At this temperature, the localization parameters of the atoms in the transverse (on the lattice) and axial (perpendicular to the lattice) directions of the trap are $\sigma_x = \sigma_y = 0.14$ μm and $\sigma_z = 0.75$ μm, respectively. A qubit is encoded in the hyperfine clock states of the atom,

$$|0\rangle := |6\mathrm{s}_{1/2}, f = 3, m_f = 0\rangle,$$
$$|1\rangle := |6\mathrm{s}_{1/2}, f = 4, m_f = 0\rangle, \tag{3}$$

with a frequency separation of 9.2 GHz, and $T_1 = 4$ s and $T_2^* = 3.5$ ms. The transition between $|1\rangle$ and the Rydberg state $|\mathrm{r}\rangle = |75\mathrm{s}_{1/2}, m_j = -1/2\rangle$ is carried out using a two-photon excitation via an intermediate state

$$|\mathrm{p}\rangle := |7\mathrm{p}_{1/2}\rangle, \tag{4}$$

with a radiative lifetime of $\tau_{7\mathrm{p}_{1/2}} = 0.155$ μs.

A CZ_ϕ gate (2) based on the simultaneous-driving procedure is implemented on a pair of atoms separated by $3d$. Each atom is irradiated by two lasers, which are focused on the atom using acousto-optic deflectors. The off-resonant two-photon transition between $|1\rangle$ and $|\mathrm{r}\rangle$ is realized using a blue-detuned (B) σ_+ laser of wavelength $\lambda_\mathrm{B} = 459$ nm for $|1\rangle \leftrightarrow |\mathrm{p}\rangle$ and a red-detuned (R) σ_- laser of wavelength $\lambda_\mathrm{R} = 1040$ nm for $|\mathrm{p}\rangle \leftrightarrow |\mathrm{r}\rangle$. We denote laser pulses for two- and one-photon excitation by $\ell = \mathrm{B,R}$, and $\ell = 0$. The detuning from $|\mathrm{p}\rangle$ is high ($\approx$760 MHz) to reduce scattering. These two beams counterpropagate along the trap's axial direction with an effective wave vector

$$k_\mathrm{eff}^\mathrm{q} := {}^{2\pi}/_{\lambda_\mathrm{B}} - {}^{2\pi}/_{\lambda_\mathrm{R}} = 7.64\ \mu\mathrm{m}^{-1}, \tag{5}$$

where the superscript "q" denotes the two-photon transition. The beam waist ($1/e^2$ intensity radius) of each laser is $w_{\mathrm{B(R)}} = 3$ μm, which results in negligible Rabi frequencies at the neighboring sites. The effective Rabi frequency for each atom is 1.7 MHz and ${}^{B}/_{2\pi} = 3$ MHz for the atom pair, which violates the Rydberg-blockade condition.

The performance of the gate is measured in terms of F_g and T_g. All atoms in the trap are initially prepared in state $|1\rangle$ by optical pumping and then undergo ${}^{\pi}/_{2}$ rotations by a global microwave pulse of frequency 9.2 GHz. The CZ_ϕ gate is then implemented by using Rydberg-excitation lasers acting on both atoms with individual addressing. The extra phase of ϕ is compensated by introducing a Stark shift to $|1\rangle$ using the blue-detuned σ_+ laser. A final ${}^{\pi}/_{2}$ rotation of the target qubit is effected by a combination of the global microwave pulse and the focused σ_+ laser. This sequence of one- and two-qubit operations prepares a Bell state with fidelity $F_\mathrm{g} \sim 0.955$, which is estimated by measuring populations of $|00\rangle$ and $|11\rangle$ and the coherence between them. This value of fidelity is reported after removing state-preparation-and-measurement (SPAM) errors and errors in single-qubit operations. Additionally, this gate implementation reports $T_\mathrm{g} = 0.8$ μs. This completes our explanation of this state-of-the-art experiment [11].

B. Adiabatic Rydberg-blockade gate in simulation

In this subsection we provide salient background on how a two-qubit neutral-atom gate is achieved by employing adiabatic Rydberg blockade. First, we briefly discuss two proposals for adiabatic population transfer using off-resonant laser pulses acting on a single atom. Next, we explain how such a population transfer, along with Rydberg-blockade interaction, realizes a CZ_ϕ gate in a pair of atoms. We then present the Hamiltonian whose evolution generates this gate. Finally, we state the estimated performance of this gate based on numerical simulation.

Two common techniques for adiabatic population transfer in a two-level atom are adiabatic rapid passage (ARP) and stimulated Raman adiabatic passage (STIRAP) [33]. The ARP technique, as first studied in the field of nuclear magnetic resonance, involves slowly sweeping the frequency of the electromagnetic field (ω) or the atomic energy separation (ω_0) across resonance [34]. The condition for this phenomena is [35]

$${}^{\Omega_1}/_{T_2} \ll \frac{d}{dt}|\omega - \omega_0| \ll \Omega_1^2, \tag{6}$$

where T_2 is the transverse relaxation time and Ω_1 is the Rabi frequency for the field. On the other hand, STIRAP is a two-photon excitation process relying on a pair of off-resonant coherent pulses, which are partially overlapping and applied counterintuitively on the atom [36].

Population transfer, via ARP, between $|1\rangle$ and $|\mathrm{r}\rangle$ is typically executed by a slowly varying chirped laser pulse applied for a duration T [37]. This Rydberg-excitation pulse, labeled by $\ell = 0$, is associated with time-dependent Rabi frequency $\Omega e^{i\varphi}$ and detuning Δ satisfying the adiabatic condition

$$\dot{\Theta} \ll \sqrt{\Omega^2 + \Delta^2}/2\pi, \quad \Theta := \tan^{-1}{}^{\Omega}/_{\Delta}, \quad \forall t \in [0, T], \tag{7}$$

for Θ the mixing angle. The interaction-picture Hamiltonian ($\hbar \equiv 1$) for this process is

$$\frac{H^\mathrm{d}(t)}{\hbar} = \frac{\Omega}{2}[e^{i\varphi}|1\rangle\langle \mathrm{r}| + e^{-i\varphi}|\mathrm{r}\rangle\langle 1|] + \frac{\Delta}{2}[|\mathrm{r}\rangle\langle \mathrm{r}| - |1\rangle\langle 1|], \tag{8}$$

where Ω incorporates the slowly varying envelope of the pulse and Δ describes its chirping.

In STIRAP, a pair of overlapping laser pulses is used to drive the $|1\rangle \leftrightarrow |\mathrm{r}\rangle$ transition by virtually employing an intermediate state $|\mathrm{p}\rangle$ [36]. One blue-detuned laser pulse driving $|1\rangle \leftrightarrow |\mathrm{p}\rangle$ and one red-detuned laser pulse driving $|\mathrm{p}\rangle \leftrightarrow |\mathrm{r}\rangle$, denoted by $\ell = \mathrm{B}$ and $\ell = \mathrm{R}$, respectively, are applied to the atom for a total duration T. Associating the laser ℓ with a time-dependent Rabi frequency Ω_ℓ and time-dependent detuning Δ_ℓ, this system is described by a Hamiltonian

$$\begin{aligned} H^\mathrm{q}(t) = {} & \frac{1}{2}(\Omega_\mathrm{B}|\mathrm{p}\rangle\langle 1| + \Omega_\mathrm{R}|\mathrm{r}\rangle\langle \mathrm{p}|) + \mathrm{H.c.} \\ & + \Delta_\mathrm{B}|\mathrm{p}\rangle\langle \mathrm{p}| + \Delta_\mathrm{BR}|\mathrm{r}\rangle\langle \mathrm{r}|, \end{aligned} \tag{9}$$

where the two-photon detuning $\Delta_\mathrm{BR} := \Delta_\mathrm{B} - \Delta_\mathrm{R}$. Using a pair of counterintuitive and partially overlapping pulses with two-photon resonance, this system adiabatically follows the dark eigenstate of $H^\mathrm{q}(t)$. This process yields a highly efficient population inversion between $|1\rangle$ and $|\mathrm{r}\rangle$, with negligible excitation of $|\mathrm{p}\rangle$. Additionally, an adiabatic elimination of $|\mathrm{p}\rangle$, under the condition

$$|\Delta_\mathrm{B}| \gg |\Omega_\mathrm{B}|, |\Omega_\mathrm{R}|, \ \forall t \in [0, T], \tag{10}$$

yields an effective two-level description for $H^\mathrm{q}(t)$ [38].

The adiabatic-gate procedure involves simultaneously driving a pair of atoms using a double pulse sequence that returns the atoms to their initial state with conditional phase accumulation [39]. This pulse sequence is symmetric about $t = {}^{T_\mathrm{g}}/_{2}$ and constructed by concatenating two adiabatic pulses, with each applied for half the gate time, i.e., $T = {}^{T_\mathrm{g}}/_{2}$. In the two-qubit computational basis, this procedure yields a

controlled-phase gate with the unitary operation

$$U(T_g) = |00\rangle\langle 00| + e^{i\phi_{01}}|01\rangle\langle 01| + e^{i\phi_{10}}|10\rangle\langle 10| + e^{i\phi_{11}}|11\rangle\langle 11|, \tag{11}$$

where $\phi_{\iota\jmath}$ is the phase accumulated by $|\iota\jmath\rangle$ over T_g. The phases satisfy $\phi_{01} = \phi_{10} = \pi$ if the shapes of the two pulses in a double-ARP sequence are identical, whereas $\phi_{01} = \phi_{10} = 0$ for a double-STIRAP sequence as $|10\rangle$ and $|01\rangle$ are dark states with zero eigenenergies [33]. Intensities and detunings of the lasers are carefully designed to ensure that $\phi_{11} = \pi$, and to consequently execute CZ_π and CZ_0 (= CZ) operations (2) with double-ARP and double-STIRAP sequences, respectively. We denote these two gates as ARP CZ_π gate and STIRAP CZ gate.

In simulation, an adiabatic Rydberg-blockade gate is executed by solving the two-atom dynamics over T_g. Typically, the effective contribution of all ground hyperfine levels, besides $|0\rangle$ and $|1\rangle$, to the dynamics is modeled as a decay channel to a single ground state [26], which we denote as $|\mathrm{g}\rangle$. The two-atom system is mathematically described by the Hamiltonian [26]

$$H_B^e(t) = H^e(t) \otimes \mathbb{1} + \mathbb{1} \otimes H^e(t) + B|\mathrm{rr}\rangle\langle \mathrm{rr}|, \tag{12}$$

where the label $\mathrm{e} = \mathrm{d}$ for the one-photon case (8) and $\mathrm{e} = \mathrm{q}$ for the two-photon case (9), with $\varphi = 0$ and a constant B satisfying the Rydberg-blockade condition

$$B \gg \Omega, \Omega_B, \Omega_R, \ \forall t \in [0, T_g]. \tag{13}$$

This condition ensures that for an initial state $|11\rangle$, the two-atom system undergoes one cycle of efficient population transfer between $|11\rangle$ and the symmetric state

$$|+\rangle := \frac{|1\mathrm{r}\rangle + |\mathrm{r}1\rangle}{\sqrt{2}}, \tag{14}$$

with a negligible population in $|\mathrm{rr}\rangle$, and the antisymmetric state $|-\rangle := \frac{|1\mathrm{r}\rangle - |\mathrm{r}1\rangle}{\sqrt{2}}$ being uncoupled to the rests.

The above gate procedure is predicted to yield robust and high-fidelity adiabatic gates on a pair of neutral alkali atoms [26,40]. Greedy optimization over pulse parameters predicts $F_g \sim 0.98$ with ARP pulses [40]. A numerical analysis of this gate procedure, with Cs atomic parameters and decay from excited levels, yields $F_g = 0.998$ over $T_g = 1$ μs using globally optimized STIRAP-inspired pulses [26]. Furthermore, this analysis predicts $F_g = 0.9994$ over $T_g = 0.54$ μs for ARP pulses. Although these gates have high fidelities, they are fundamentally slow due to the use of adiabatic pulses.

C. Estimating fidelity in simulation

Here we discuss the typical procedures for simulating the generation of an approximate Bell state and estimating the state fidelity for two cases, namely, with and without technical imperfections and spontaneous emission. We use the term "imperfections" to refer to fluctuations of laser intensity, atomic position and detunings, which are in turn affected by magnetic-field and temperature variations. We start by introducing the sequence of operations that prepares an ideal Bell state and then define fidelity of a nonideal state generated by this sequence. Next, we elaborate on the process of generating the requisite evolution for a two-qubit operation using the two-atom Hamiltonian. At the end, we discuss how to incorporate parameter fluctuations into the Hamiltonian dynamics.

A Bell state is generated from the ground state $|11\rangle$ using a sequence of single- and two-qubit gate operations. The two-atom system is initially prepared in an equal superposition of the computational basis states as

$$|\psi_0\rangle = \frac{(|0\rangle - |1\rangle) \otimes (|0\rangle - |1\rangle)}{2} \tag{15}$$

by applying Hadamard (H) gates to each of the qubits in $|11\rangle$, which are denoted as control and target, respectively. The final state $|\psi_f\rangle$, which ideally is a Bell state [12]

$$|\beta_{\iota\jmath}\rangle := (|0, \jmath\rangle + (-1)^\iota |1, 1-\jmath\rangle)/\sqrt{2}, \quad \forall \iota, \jmath \in \{0, 1\}, \tag{16}$$

is then prepared from $|\psi_0\rangle$ by first applying a controlled-phase gate and then another H gate to the target qubit. Particularly, ideal CZ and CZ_π gates yield the Bell states $|\beta_{11}\rangle$ and $|\beta_{00}\rangle$, respectively [26].

The Bell-state preparation fidelity is defined as the overlap between the final two-atom state $|\psi_f\rangle$ and the corresponding ideal Bell-state $|\beta_{\iota\jmath}\rangle$. Under assumptions of ideal and instantaneous H gates and nonideal controlled-phase gate, which incorporates only the fundamental imperfection due to finite B, the intrinsic fidelity of the given controlled-phase gate is

$$F_g^0 := F_{\iota\jmath}^0 = |\langle \beta_{\iota\jmath}|\psi_f\rangle|^2, \tag{17}$$

where $F_{\iota\jmath}^0$ is the intrinsic Bell-state preparation fidelity. Furthermore, the realistic fidelity F_g is measured in terms of the realistic Bell-state preparation fidelity $F_{\iota\jmath}$ as

$$F_g := F_{\iota\jmath} = \langle \beta_{\iota\jmath}|\rho_f|\beta_{\iota\jmath}\rangle, \tag{18}$$

where ρ_f denotes the final density matrix of the two-atom system obtained via nonunitary dynamics in the presence of decay and imperfections. In the following, we explain how realistic gate operations are derived from open-system evolutions.

The evolution of a time-dependent Hamiltonian, which represents the dynamics of a coupled two-atom system, over time T_g yields a two-qubit entangling gate. For an interaction picture Hamiltonian H, two-atom density matrix $\rho(t)$ and a "superoperator" $\mathscr{L}[\rho(t)]$, the dynamics of a Rydberg-blockade gate is simulated by integrating the two-atom Gorini-Kossakowski-Sudarshan-Lindblad (GKSL) equation [26,41–43]

$$\frac{d\rho(t)}{dt} = i[\rho(t), H] + \mathscr{L}[\rho(t)] \otimes \mathbb{1} + \mathbb{1} \otimes \mathscr{L}[\rho(t)]. \tag{19}$$

The superoperator for all decay channels is

$$\mathscr{L}[\rho(t)] := \sum_{j,k<j} c_{jk}\rho(t)c_{jk}^\dagger - \frac{1}{2}\{c_{jk}^\dagger c_{jk}, \rho(t)\}, \tag{20}$$

where $\{,\}$ denotes an anticommutator and the collapse operator

$$c_{jk} := \sqrt{b_{jk}\gamma_j}|k\rangle\langle j| \tag{21}$$

denotes the radiative decay channel from a higher energy state $|j\rangle$ to a lower energy state $|k\rangle$ with a decay rate $b_{jk}\gamma_j$. The total decay rate from $|j\rangle$ is γ_j and the coefficient b_{jk}, called

branching ratio, denotes the fraction of decay to one of the lower energy states. Particularly, for each atom, the relevant high-energy states are $|\mathrm{r}\rangle$ and $|\mathrm{p}\rangle$ with decay rates γ_r and γ_p, respectively, where the latter has a dominant contribution to a two-photon Rydberg excitation process [9,32].

To account for imperfections in quantum gate operations, Monte Carlo (MC) simulation of the GKSL equation (19) is performed with realistic parameter fluctuations [41–43]. These imperfections include thermal motion of atoms in traps, laser (intensity and phase) fluctuation, Doppler dephasing of Rydberg state, magnetic field fluctuations and dynamic Stark shifts of atomic energy levels. A detailed analysis of these technical imperfections shows that the dominant gate errors are atomic motion and dephasing, which arise predominantly due to nonzero atomic temperature [32]. Below we describe modeling of fluctuations in the Rabi frequency and detuning of each Rydberg-excitation laser, and finally explain how to estimate fidelity from MC simulation.

The two major sources of Rabi-frequency fluctuations are atomic temperature and laser-intensity fluctuations. The atomic position $\boldsymbol{r} := (x, y, z)$ at each trap site varies according to normal distributions as [42]

$$x \sim \mathcal{N}\big(0, \sigma_x^2\big), \quad y \sim \mathcal{N}\big(0, \sigma_y^2\big), \quad z \sim \mathcal{N}\big(0, \sigma_z^2\big), \tag{22}$$

where σ_x, σ_y, and σ_z depend on trap parameters and atomic temperature. These variations, along with the minimum beam waist w_ℓ of the Rydberg-excitation laser ℓ, lead to fluctuations in the spatial form factor [32,42]

$$p_\ell(\boldsymbol{r}) = \frac{e^{-\frac{x^2+y^2}{w_\ell^2\left(1+z^2/L_\ell^2\right)}}}{\sqrt{1+z^2/L_\ell^2}} \tag{23}$$

of the Rabi frequency, where the corresponding Rayleigh length $L_\ell := \pi w_\ell^2/\lambda_\ell$. Additionally, a laser-intensity fluctuations is modeled as the factor [41–43]

$$f_\ell \sim \sqrt{1+\mathcal{N}\big(0, \big(\sigma_\ell^\mathrm{i}\big)^2\big)}, \tag{24}$$

with σ_ℓ^i being the standard deviation of intensity for the laser ℓ.

The dephasing of the Rydberg state relative to the ground state arises mainly due to the Doppler effect and magnetic-field variation [44]; this dephasing process is modeled as fluctuations in laser detuning [42]. For atomic mass M_a and Boltzmann constant k_B, the dephasing rate due to the Doppler effect is [42–44]

$$\sigma^{\mathrm{D,e}} = \sqrt{2}\big(T_2^{\mathrm{D,e}}\big)^{-1} := \sqrt{2}\left(\frac{\sqrt{2M_\mathrm{a}/k_\mathrm{B}T_\mathrm{a}}}{k_\mathrm{eff}^\mathrm{e}}\right)^{-1}, \tag{25}$$

where $k_\mathrm{eff}^\mathrm{d} := 2\pi/\lambda_0$. In the presence of a magnetic field fluctuating with a standard deviation σ_B and a Rydberg state with magnetic quantum number m_j, the dephasing rate [42,44]

$$\sigma^{\mathrm{m,e}} = \sqrt{2}\big(T_2^{\mathrm{m,e}}\big)^{-1} := \sqrt{2}\left(\frac{2^{3/2}\pi\hbar}{|g_\mathrm{r} m_j - g_1 m_f|\mu_\mathrm{B}\sigma_\mathrm{B}}\right)^{-1}, \tag{26}$$

for $g_1 m_f = 0$ (3). These two decoherence processes are then modeled as random shifts [42,43]

$$\Delta_\mathrm{D} \sim \mathcal{N}(0, (\sigma^{\mathrm{D,e}})^2), \quad \Delta_\mathrm{m} \sim \mathcal{N}(0, (\sigma^{\mathrm{m,e}})^2) \tag{27}$$

of the Rydberg-level detuning for Doppler sensitivity and magnetic sensitivity, respectively. Other sources for this decoherence include laser phase noise [43] and a finite value for γ_r [32], where the latter is already included in c_{rk} (21).

MC simulation of a quantum gate involves solving the GKSL equation (19) multiple times using different values for Hamiltonian coefficients, and reporting the average solution [41–43]. To account for atomic-position and laser-intensity fluctuations in each MC run, the time-dependent Rabi frequency function for each laser ℓ is multiplied by two values sampled from $p_\ell(\boldsymbol{r})$ and f_ℓ. Furthermore, random samples from Δ_D and Δ_B are added to the time-dependent detuning in order to include dephasing effects in every MC run. The estimated fidelity in the presence of spontaneous emission and these imperfections is the average of fidelities calculated in all MC runs by solving the corresponding GKSL equation and evaluating F_g (18).

D. Transitionless quantum driving

TQD is an alternative to using adiabatic pulses and narrow-band on-resonant pulses for efficient population transfer between atomic energy levels [28,45]. In this subsection, we summarize relevant background on TQD and its applications to quantum control. We begin by introducing the control Hamiltonian and the TQD Hamiltonian for a general quantum system. Next, we provide expressions of the control and TQD Hamiltonians for a two-level system and discuss possible experimental realizations for this TQD Hamiltonian. Finally, we state examples of quantum-control problems that employ this technique.

In TQD the quantum system follows the instantaneous eigenstates of an adiabatic Hamiltonian for all integration times. Given an adiabatic $H(t)$ with instantaneous eigenstates $\{|E(t)\rangle\}$ and corresponding eigenenergies $\{\epsilon(t)\}$, the transitionless dynamics is achieved by adding a TQD control Hamiltonian [28]

$$H_\mathrm{c}(t) = \mathrm{i}\sum_E \big(|\dot{E}(t)\rangle\langle E(t)| - \langle E(t)|\dot{E}(t)\rangle |E(t)\rangle\langle E(t)|\big) \tag{28}$$

to $H(t)$. The resultant TQD Hamiltonian

$$\check{H}(t) = H(t) + H_\mathrm{c}(t) \tag{29}$$

nonadiabatically drives the system along an adiabatic path of $H(t)$ by effectively canceling the transitions between $\{|E(t)\rangle\}$. This technique, which we refer to as the "TQD technique," is often used as a quantum control tool for speeding up adiabatic processes.

The TQD technique has been applied to an ARP Hamiltonian to speed up population inversion between ground and excited levels of a two-level system [46]. To this end, the control Hamiltonian is calculated using two eigenstates. For the two-level atomic system described by $H^\mathrm{d}(t)$ (8), the eigenstates are

$$\begin{aligned} |E_+(t)\rangle &= \cos\Theta/2|1\rangle + e^{\mathrm{i}\varphi}\sin\Theta/2|\mathrm{r}\rangle, \\ |E_-(t)\rangle &= -\sin\Theta/2|1\rangle + e^{\mathrm{i}\varphi}\cos\Theta/2|\mathrm{r}\rangle, \end{aligned} \tag{30}$$

and their corresponding eigenenergies are

$$\epsilon_\pm(t) = \pm\sqrt{\Delta^2+\Omega^2}/2. \tag{31}$$

Assuming a time-independent φ and assigning $\Omega_c = \dot{\Theta}$, the control Hamiltonian (28) is then derived as

$$H_c^d(t) = -ie^{i\varphi}\frac{\Omega_c}{2}|1\rangle\langle r| + \text{H.c.} \tag{32}$$

In a basis spanned by $\{|E_\pm(t)\rangle\}$, only the off-diagonal terms of this Hamiltonian are nonzero, which signifies that the impact of $H_c^d(t)$ is to counteract the nonadiabatic couplings of the eigenstates of $H^d(t)$.

The TQD Hamiltonian for the two-level system is then calculated by adding $H_c^d(t)$ to $H^d(t)$ and is experimentally realized by either using an additional laser [46] or modifying the existing laser [47]. Mathematically, the TQD of a two-level system is represented by

$$\check{H}^d(t) = \frac{e^{i\varphi}}{2}(\Omega - i\Omega_c)|1\rangle\langle r| + \text{H.c.} + \frac{\Delta}{2}[-|1\rangle\langle 1| + |r\rangle\langle r|], \tag{33a}$$

$$\xrightarrow{U_\theta(t)} \frac{\Omega'}{2}[e^{i\varphi}|1\rangle\langle r| + e^{-i\varphi}|r\rangle\langle 1|] + \frac{\Delta'}{2}[|r\rangle\langle r| - |1\rangle\langle 1|], \tag{33b}$$

where

$$\Omega' := \sqrt{\Omega^2 + \Omega_c^2}, \quad \Delta' := \Delta + \dot{\theta}, \tag{34}$$

for $\theta := \tan^{-1}\Omega_c/\Omega$, and Eq. (33b) is derived from Eq. (33a) by appropriate unitary transformation using $U_\theta(t) := \text{diag}(1, e^{i\theta})$. The implementation of Eq. (33a) employs two lasers with the same frequency, orthogonal polarization and different time-dependent functions for intensities, whereas Eq. (33b) is realized by modifying the time-dependent intensity and detuning of the original laser. A geometric interpretation for TQD of a similar two-level system, i.e., a spin 12 particle in a rotating magnetic field, using trajectories on a Bloch sphere is also provided [48].

Quantum control based on TQD has been used to transfer population between atomic states, create entangled states and design quantum gates in short times [49–54]. A particular experiment demonstrates a robust population transfer in cold neutral atoms using TQD STIRAP, which is faster than conventional STIRAP [55]. This work also highlights the speed-up limit of TQD over adiabatic driving and compares the resource requirement for both processes. Another work proposed a procedure for generating a three-qubit entangled state in Rydberg atoms using TQD and ground-state blockade mechanism [56]. Motivated by these theoretical and experimental works, we use the TQD technique to speed up adiabatic Rydberg-blockade gates.

III. APPROACH

In this section, we discuss our approach for designing a CZ_ϕ (2) gate using our modified TQD technique and assessing the gate performance. We begin by explaining our detailed model for the two-atom system, including effects of spontaneous emission and technical imperfections. Then we mathematically describe our gate procedure. Finally, we elaborate on our numerical simulation for the two-qubit gate.

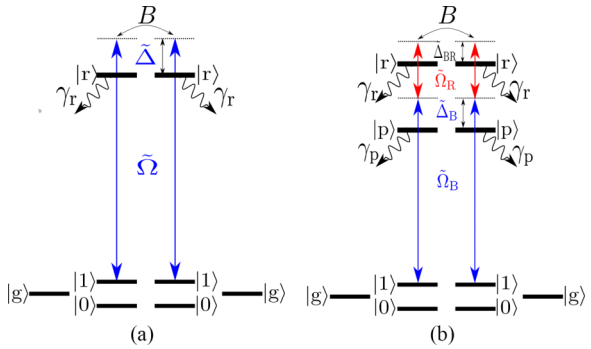

FIG. 1. A pair of Cs atoms driven by detuned, broadband laser pulses. (a) Each atom is excited to its Rydberg level $|r\rangle$ by a one-photon excitation process with time-dependent Rabi frequency $\tilde{\Omega}$ and detuning $\tilde{\Delta}$. The decay rate γ_r of state $|r\rangle$ is $1/593\ \mu s^{-1}$ with branching ratios $b_{r0} = b_{r1} = 1/16$ and $b_{rg} = 7/8$. The blockade shift between the atoms is 3 GHz. (b) Each atom is excited by a two-photon excitation process, with time-dependent $\tilde{\Omega}_B$ and $\tilde{\Omega}_R$, via the intermediate state $|p\rangle$ and single-photon detuning $\tilde{\Delta}_B$. The two-photon detuning $\tilde{\Delta}_{BR} := \tilde{\Delta}_B - \tilde{\Delta}_R$. The decay rate γ_r is $1/367\ \mu s^{-1}$, and the decay rate γ_p of state $|p\rangle$ is $1/0.155\ \mu s^{-1}$ with branching ratios $b_{r0} = b_{r1} = 1/32$, $b_{rg} = 7/16$ and $b_{rp} = 1/2$. The blockade shift between the atoms is 2 GHz. Other relevant parameters and their values are provided in Table I.

A. Model

We adapt the model for a pair of laser-driven neutral atoms [26] and make our model comprehensive by incorporating spontaneous emission and major technical imperfections [11,32]. Here we first present our model for two trapped atoms whose positions fluctuate due to nonideal trapping conditions. For each of these atoms, we then consider two different physical processes, namely, two types of Rydberg-excitation processes, one for one-photon and the other for two-photon driving. We use numerical values for the atomic and experimental parameters that are feasible with state-of-the-art instruments; see Table I.

We consider two cold ($T_a = 5\ \mu K$ [11]) Cs atoms trapped in an optical lattice at a separation $\leqslant 3.4\ \mu m$ and experiencing a strong dipole-dipole interaction of strength $B/2\pi \geqslant 2\,GHz$ between them. Each atom is described as a five-level system corresponding to the qubit basis states $|0\rangle$ and $|1\rangle$ (3), effective ground state $|g\rangle$, intermediate exited state $|p\rangle$ (4), which is relevant only for two-photon driving, and a Rydberg state $|r\rangle$ (Fig. 1). We choose the atomic level with principal quantum number 112 as $|r\rangle$ in our simulations, where the exact choice for the orbital quantum number depends on the excitation process [42]. We neglect decoherence of the ground hyperfine levels, whose T_1 and T_2^* are orders of magnitude greater than other relaxation times of the system (Sec. II A), but consider radiative decay of the excited levels $|p\rangle$ and $|r\rangle$. The positional uncertainty of each atom at each trap site follows a three-dimensional Gaussian distribution, about the trap center, with standard deviations $\sigma_x = \sigma_y = 0.24\ \mu m$ and $\sigma_z = 0.92\ \mu m$ [11]. Additionally, we assume ideal optical pumping, hyperfine transitions, and state detection because errors from SPAM and fast single-qubit gates are typically accounted for when estimating fidelities in experiments [9,11,32].

TABLE I. Atomic and experimental parameters used in our simulations.

	Laser				Rydberg state			Rydberg blockade	
Excitation	Wavelength	Wave vector	Waist	Rayleigh length	Atomic level	g_j	Lifetime	$B/2\pi$	Distance
One-photon	$\lambda_0 = 319$ nm	19.7 μm^{-1}	$w_0 = 2.5$ μm	$L_0 = 61.5$ μm	$\lvert 112p_{3/2}, m_j = 3/2\rangle$	4/3	593 μs	3 GHz	3.05 μm
Two-photon	$\lambda_B = 459$ nm	7.63 μm^{-1}	$w_B = 3$ μm	$L_B = 61.6$ μm	$\lvert 112d_{5/2}, m_j = 5/2\rangle$	6/5	367 μs	2 GHz	3.4 μm
	$\lambda_R = 1038$ nm		$w_R = 3$ μm	$L_R = 27.2$ μm					

In the one-photon-excitation model for a trapped Cs atom, the $|1\rangle \leftrightarrow |r\rangle$ transition of both atoms is driven simultaneously using an off-resonant, broadband laser, which is associated with a time-dependent Rabi frequency $\tilde{\Omega}(t)$ and detuning $\tilde{\Delta}(t)$; see Fig. 1(a). Our model can be implemented using an ultraviolet laser of wavelength $\lambda_0 = 319$ nm [29,57] simultaneously focused on both atoms by an advanced beam-scanning mechanism [11]. In order to safely neglect crosstalk errors, we use a beam waist of $w_0 = 2.5$ μm and interatomic distance of 3.05 μm in our simulations. We consider a 5% fluctuation of the laser intensity, $\sigma_0^i = 0.05\,(24)$, but neglect phase noise because of the current experimental improvements in resonant filtering [58]. A strong Rydberg blockade with $B/2\pi = 3$ GHz is achieved between the atom pair by our choice of

$$|r\rangle = |112p_{3/2}, m_j = 3/2\rangle \tag{35}$$

with a decay rate [42] (branching ratios)

$$\gamma_r = 1/593\,\text{MHz}\ (b_{r0} = b_{r1} = 1/16,\ b_{rg} = 7/8). \tag{36}$$

Additionally, we simulate dephasing of $|r\rangle$ with respect to $|1\rangle$ using $T_2^{D,d} = 4$ μs (25) and $T_2^{m,d} = 50$ μs (26), for $\sigma_B = 10^{-6}$ T [32].

In the two-photon transition model, both Cs atoms are simultaneously driven between their ground and Rydberg states using a pair of partially overlapping laser pulses [26]. This model has been realized using narrowband pulses applied to a 2D lattice [11,32]. We describe the effect of the blue(red)-detuned laser, having $\lambda_{B(R)} = 459(1040)$ nm, on the $|1\rangle(|p\rangle) \leftrightarrow |p\rangle(|r\rangle)$ transition by time-dependent Rabi frequency $\tilde{\Omega}_{B(R)}(t)$ and detuning $\tilde{\Delta}_{B(R)}(t)$; see Fig. 1(b). Each of these two Rydberg-excitation lasers is broadband with a finite beam waist of $w_{B(R)} = 3$ μm. By choosing an interatomic distance of 3.4 μm and

$$|r\rangle = |112d_{5/2}, m_j = 5/2\rangle, \tag{37}$$

we simulate a strong blockade with $B/2\pi = 2$ GHz. We consider spontaneous emission from the two excited levels $|p\rangle$ and $|r\rangle$, with decay rates (branching ratios) [42]

$$\begin{aligned}\gamma_p &= 1/\tau_{7p_{1/2}}\ (b_{p0} = b_{p1} = 1/16,\ b_{pg} = 7/8),\\ \gamma_r &= 1/367\,\text{MHz}\ (b_{r0} = b_{r1} = 1/32,\ b_{rg} = 7/16,\ b_{rp} = 1/2),\end{aligned} \tag{38}$$

respectively. Additional imperfections arising from laser-intensity fluctuations, Doppler effect, and magnetic field fluctuations are modeled using parameters $\sigma_{B,R}^i = 0.01$ [59], $T_2^{D,q} = 10.5$ μs, and $T_2^{m,q} = 34$ μs, respectively.

B. Mathematics

In this subsection, we explain the mathematics behind designing and characterizing a CZ_ϕ gate (2). We begin by providing a valid Hamiltonian representation for our laser-driven two-atom model (Sec. III A) and then discuss how we decompose the Hamiltonian into a direct sum. Next, we elaborate our procedure to derive time-dependent coefficients for this Hamiltonian, such that the resultant unitary dynamics yields a ground-Rydberg entangled state for an integration time that is faster than the adiabatic timescale. As this dynamics is only necessary but not sufficient to achieve a high-fidelity, fast CZ_ϕ operation, we propose a recipe to design each time-dependent laser beam as a sequence of phase-shifted pulses. Finally, we introduce our metric to evaluate a CZ_ϕ gate.

For each of the two Rydberg-excitation models, i.e., one- and two-photon, we generalize the respective single-atom Hamiltonians $H^e(t)$ (8), (9) to account for imperfections in the $|1\rangle \leftrightarrow |r\rangle$ transition. To this end, we assume nonadiabatic parametrization for the time-dependent coefficients and include additional coefficients describing parameter fluctuations. The one-photon form of this space-time-dependent Hamiltonian $\tilde{H}^e(t, \boldsymbol{r})$ is

$$\begin{aligned}\tilde{H}^d(t, \boldsymbol{r}) = &\frac{1}{2} p_0(\boldsymbol{r}) f_0 \tilde{\Omega}(t) |1\rangle\langle r| + \text{H.c.}\\ &+ \frac{\tilde{\Delta}(t) + \Delta_m + \Delta_D}{2} [|r\rangle\langle r| - |1\rangle\langle 1|],\end{aligned} \tag{39}$$

where fluctuations in Rabi frequency and detuning are described by $p_0(\boldsymbol{r}) f_0$ [(23) and (24)] and random shifts $\Delta_m + \Delta_D$ (27), respectively. Similarly, for the two-photon transition,

$$\begin{aligned}\tilde{H}^q(t, \boldsymbol{r}) = &\frac{1}{2} p_B(\boldsymbol{r}) f_B \tilde{\Omega}_B(t) |p\rangle\langle 1| + \frac{1}{2} p_R(\boldsymbol{r}) f_R \tilde{\Omega}_R(t) |r\rangle\langle p|\\ &+ \text{H.c.} + \tilde{\Delta}_B(t) |p\rangle\langle p|\\ &+ \left(\tilde{\Delta}_{BR}(t) + \Delta_m + \Delta_D\right) |r\rangle\langle r|,\end{aligned} \tag{40}$$

where we assume $\tilde{\Delta}_{BR} \approx 0$ and a high $\tilde{\Delta}_B$ satisfying the adiabatic elimination condition (10).

Our model for a pair of interacting atoms is thus mathematically represented by a space-time-dependent Hamiltonian, which is valid for our gate procedure under the following three conditions. This two-atom Hamiltonian

$$\tilde{H}_B^e(t, \boldsymbol{r}) = \tilde{H}^e(t, \boldsymbol{r}) \otimes \mathbb{1} + \mathbb{1} \otimes \tilde{H}^e(t, \boldsymbol{r}) + B |rr\rangle\langle rr|, \tag{41}$$

whose time-dependent coefficients follow the Rydberg-blockade condition (13), acts on a 25-dimensional Hilbert space $\mathscr{H}$. To describe a valid CZ_ϕ operation over time T_g, our gate procedure requires $\tilde{H}_B^e(t, \boldsymbol{r})$ to satisfy the following conditions:

C1. Unitary evolution generated by $\tilde{H}^{\rm e}_{\rm B}(t,\boldsymbol{r})$, in the absence of parameter fluctuations, yields an efficient population transfer back to the same initial state $|11\rangle$ over any $T_{\rm g}$.

C2. Unitary dynamics for an initial state $|10\rangle$ also yields an efficient population transfer back to the same initial state over any $T_{\rm g}$.

C3. Final accumulated phases of initial states belonging to the two-qubit computational basis (11) must satisfy the relation

$$\phi_{11} - 2\phi_{10} = (2n+1)\pi,\ \forall n \in \mathbb{Z}. \tag{42}$$

These conditions together ensure the implementation of a high-fidelity CZ_ϕ gate.

We can decompose this 25-dimensional $\tilde{H}^{\rm e}_{\rm B}(t,\boldsymbol{r})$ into a direct sum of one- and two-dimensional Hamiltonians; see the Appendix for details. This is achieved by first identifying the nine-dimensional subspace $\mathscr{H}_{\rm CZ}$, spanned by $\{|0\rangle, |1\rangle, |{\rm r}\rangle\}$ of both atoms and decoupled from their other states, which captures the physics of a CZ_ϕ gate. This nine-dimensional subspace further decomposes as

$$\begin{aligned} 9 &= 1\oplus 2\oplus 2\oplus 4 \approx 1\oplus 2\oplus 2\oplus 2\oplus 1\oplus 1 \\ &= \underbrace{\mathrm{span}\{|00\rangle\}}_{\mathscr{H}_0} \oplus \underbrace{\mathrm{span}\{|01\rangle, |0{\rm r}\rangle\}}_{\mathscr{H}_{0{\rm r}}} \oplus \underbrace{\mathrm{span}\{|10\rangle, |{\rm r}0\rangle\}}_{\mathscr{H}_{{\rm r}0}} \\ &\quad \oplus \underbrace{\mathrm{span}\{|11\rangle, |+\rangle\}}_{\mathscr{H}_{\rm rr}} \oplus \mathrm{span}\{|-\rangle\} \oplus \mathrm{span}\{|{\rm rr}\rangle\}. \end{aligned} \tag{43}$$

Each of the two-dimensional Hamiltonians acting on $\mathscr{H}_{0{\rm r}}$ and $\mathscr{H}_{{\rm r}0}$ resembles the single-atom Hamiltonian for one-photon driving (8), whereas the two-dimensional Hamiltonian acting on $\mathscr{H}_{\rm rr}$, denoted by $\tilde{H}^{\rm e}_{\rm B,eff}(t,\boldsymbol{r})$, generates atom-atom entanglement. We formalize the mapping from $\tilde{H}^{\rm e}_{\rm B}(t,\boldsymbol{r})$ to $\tilde{H}^{\rm e}_{\rm B,eff}(t,\boldsymbol{r})$ by a "conjugating-channel" transformation as

$$\tilde{H}^{\rm e}_{\rm B,eff}(t,\boldsymbol{r}) \oplus \mathbb{0}_{23} = \mathcal{C}_R\big(\tilde{H}^{\rm e}_{\rm B}(t,\boldsymbol{r})\big), \tag{44}$$

where the conjugating channel

$$\mathcal{C}_R(\bullet) := R \bullet R^\top, \tag{45}$$

and the real-valued matrix R is a composition of projection and permutation operators.

To make TQD feasible for 25-dimensional $\mathscr{H}$, we modify the standard TQD technique (Sec. II D). Our modification involves the following: first derive a TQD Hamiltonian for a low-dimensional subspace of $\mathscr{H}$ and then map this Hamiltonian back to a full 25-dimensional matrix. This procedure yields time-dependent coefficients for $\tilde{H}^{\rm e}_{\rm B}(t,\boldsymbol{r})$ as functions of the coefficients for the adiabatic Hamiltonian $H^{\rm e}_{\rm B}(t)$ (12).

We apply the TQD technique to an adiabatic Hamiltonian acting on a low-dimensional, nontrivial subspace of $\mathscr{H}$. Here we pick $\mathscr{H}_{\rm rr}$ because Hamiltonian dynamics on this subspace is entangling. The effective Hamiltonian $H^{\rm e}_{\rm B,eff}(t)$ acting on $\mathscr{H}_{\rm rr}$ is calculated as

$$H^{\rm e}_{\rm B,eff}(t) \oplus \mathbb{0}_{23} = \mathcal{C}_R\big(H^{\rm e}_{\rm B}(t)\big), \tag{46}$$

where $\mathcal{C}_R$ (45) is justified because the graph representations of $H^{\rm e}_{\rm B}(t)$ and $\tilde{H}^{\rm e}_{\rm B}(t,\boldsymbol{r})$ are isomorphic to each other. The time-dependent coefficients of $\tilde{H}^{\rm e}_{\rm B,eff}(t,\boldsymbol{r})$, in the absence of parameter fluctuations, are then assigned functions by

$$\tilde{H}^{\rm e}_{\rm B,eff}(t,\boldsymbol{0}) \leftarrow \check{H}^{\rm e}_{\rm B,eff}(t), \tag{47}$$

where $\check{H}^{\rm e}_{\rm B,eff}(t)$ is the TQD Hamiltonian obtained from the adiabatic $H^{\rm e}_{\rm B,eff}(t)$.

We now utilize this two-dimensional $\tilde{H}^{\rm e}_{\rm B,eff}(t,\boldsymbol{r})$ to derive expressions for the time-dependent coefficients of the 25-dimensional $\tilde{H}^{\rm e}_{\rm B}(t,\boldsymbol{r})$. This derivation is achieved by the inverse operation of $\mathcal{C}_R$ (44) as

$$\tilde{H}^{\rm e}_{\rm B}(t,\boldsymbol{r}) = \mathcal{C}_R^{-1}\big(\tilde{H}^{\rm e}_{\rm B,eff}(t,\boldsymbol{r}) \oplus \mathbb{0}_{23}\big). \tag{48}$$

We refer to this constructed Hamiltonian as a "constrained-TQD Hamiltonian," where "constrained-TQD" (cTQD) signifies that the TQD technique is applied to a Hamiltonian acting on only one subspace of the full Hilbert space. Due to this unique construction, the unitary dynamics of $\tilde{H}^{\rm e}_{\rm B}(t,\boldsymbol{r})$, without parameter fluctuations, yields efficient population transfer only between $|11\rangle$ and $|+\rangle$ over any arbitrarily low integration time, thus satisfying C1.

In order to derive explicit time-dependent functions for $\tilde{H}^{\rm e}_{\rm B}(t,\boldsymbol{r})$, we use popular functions for expressing $H^{\rm e}_{\rm B}(t)$. Particularly, for describing ARP (8), we use electric field of the form of a linearly chirped Gaussian (LCG) function [33,39], with

$$\Omega(t) = \Omega_0 e^{-\frac{(t-T/2)^2}{\tau^2}}, \quad \Delta(t) = 2\Delta_0/T(t - T/2), \tag{49}$$

where the Rabi frequency is Gaussian with peak value Ω_0, mean $T/2$, and width τ, and the detuning is linear with peak value Δ_0. Furthermore, we describe STIRAP pulses (9) by Rabi frequencies with hyper-Gaussian shapes [26] as

$$\Omega_{\rm B}(t) = \Omega_{\rm B0} e^{-(t-2T/3)^4/\tau_{\rm B}^4}, \quad \Omega_{\rm R}(t) = \Omega_{\rm R0} e^{-(t-T/3)^4/\tau_{\rm R}^4}, \tag{50}$$

and a constant detuning $\Delta_{\rm B}(\equiv -\Delta_{\rm R})$, henceforth referred as zero-chirped hyper-Gaussian (ZCHG). This pair of ZCHG pulses conforms to the conditions for optimized STIRAP [60] and is also simple enough for our analytical calculations. The parameters of these functions are judiciously chosen to deliver feasible CZ_ϕ gates, as detailed in Sec. III C.

A CZ_ϕ gate implemented by evolving the cTQD Hamiltonian (48) does not guarantee high fidelity over low gate time; this deficiency motivates us to redesign pulse shapes such that C2 and C3 are satisfied as well. To do this, we start with a $H^{\rm e}_{\rm B}(t)$ whose coefficients are single-adiabatic pulse functions (49) and (50), as opposed to double-adiabatic pulses used for executing CZ and CZ_π operations (Sec. II B). Thus the time-dependent functions $\tilde{\Omega}$ and $\tilde{\Delta}$ ($\tilde{\Omega}_{\rm B}$, $\tilde{\Delta}_{\rm B}$, $\tilde{\Omega}_{\rm R}$, and $\tilde{\Delta}_{\rm R}$) are expressed in terms of LCG (ZCHG) pulse functions. We refer to these particular pulses as "TQD pulses" and represent their functions by $\tilde{\Omega}^+(t)$ and $\tilde{\Delta}^+(t)$ for the one-photon case, and by $\tilde{\Omega}^+_{\rm B}(t)$, $\tilde{\Delta}^+_{\rm B}(t)$, $\tilde{\Omega}^+_{\rm R}(t)$, and $\tilde{\Delta}^+_{\rm R}(t)$ for the two-photon case.

For implementing a high-fidelity cTQD CZ_ϕ gate over any gate time $T_{\rm g}$, we design the time-dependent coefficients of $\tilde{H}^{\rm e}_{\rm B}(t,\boldsymbol{r})$ (41) as sequences of four TQD pulse functions. To construct this sequence, we modify a gate procedure [9] by using TQD pulses, which are broadband, instead of narrowband 2π pulses. Specifically, we propose dividing a sequence of TQD pulses into two identical subsequences having a relative phase shift of $\phi_{\rm R}$ between them. For each subsequence, we employ a pair of TQD pulses, with a time-symmetric envelope and a relative phase shift $\phi_{\rm r}$, instead of restricting to a 2π pulse [9]. The pulse pair is designed such that the initial state

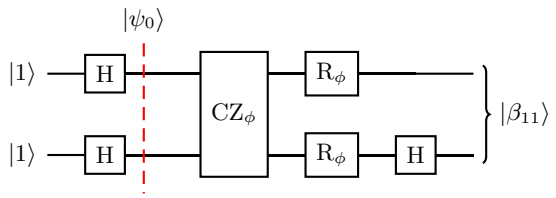

FIG. 2. A two-qubit quantum circuit for preparing the Bell state $|\beta_{11}\rangle$ (16). Both qubits are initialized to state $|1\rangle$, with upper and lower qubits acting as control and target, respectively. Each of these qubits undergo H transformation, which ideally yields $|\psi_0\rangle$. This state is then subjected to a CZ_ϕ gate (2), followed by two $R_\phi[:= \mathrm{diag}(1, e^{-i\phi})]$ gates on control and target. A final H on target ideally yields $|\beta_{11}\rangle$. This circuit is a slight modification of the one explained in Sec. II C.

$|11\rangle$ returns efficiently back to itself over an integration time of $T_g/2$, having accumulated a phase of $\phi_{11}/2$. Contrariwise, for the other two nontrivial initial states $|01\rangle$ and $|10\rangle$, this subsequence alone does not ensure efficient population transfer back to the corresponding states after $T_g/2$. By judicious choice of the parameter ϕ_R, the full sequence efficiently returns the atoms to their corresponding initial states $|01\rangle$ and $|10\rangle$ over time T_g with an accumulated phase $\phi = \phi_{10}(= \phi_{01})$, thus satisfying C2. Additionally, our choices for ϕ_r and ϕ_R ensure that ϕ_{10} and ϕ_{11} satisfy the phase relation (42) for C3.

We assess a cTQD CZ_ϕ gate by estimating the Bell-state preparation fidelity of a quantum state obtained by applying single-qubit gates and this two-qubit gate on $|11\rangle$; see Fig. 2. In each MC run (Sec. II C), we first construct a random $\tilde{H}_B^e(t, \boldsymbol{r})$ by sampling its coefficients from their respective distributions [(23), (24), and (27)] and then integrate the GKSL equation (19), with initial state $|\psi_0\rangle$ (15) and Cs decay parameters [(36) and (38)], over T_g to obtain $\rho(T_g)$.

After executing ideal and instantaneous single-qubit rotations on $\rho(T_g)$, the final state

$$\rho_f = (\mathbb{1} \otimes \mathrm{H})(\mathrm{R}_\phi \otimes \mathrm{R}_\phi).\rho(T_g)(\mathrm{R}_\phi^\dagger \otimes \mathrm{R}_\phi^\dagger)(\mathbb{1} \otimes \mathrm{H}^\dagger) \tag{51}$$

is used to calculate an estimate of the realistic fidelity [61]

$$F_g := \langle\beta_{11}|\rho_f|\beta_{11}\rangle = \frac{\rho_{0101} + \rho_{1010}}{2} + |\rho_{1001}|, \tag{52}$$

where the matrix elements are

$$\rho_{i_1 i_2 i_3 i_4} = \langle i_1 i_2|\rho_f|i_3 i_4\rangle, \quad i_1, i_2, i_3, i_4 \in \{0, 1\}. \tag{53}$$

We perform 100 MC runs to generate a distribution of fidelity estimates and use the mean to estimate the gate infidelity $1 - F_g$. Additionally, we calculate the standard error σ_F^- from this distribution, and use σ_F^- to represent robustness of the two-qubit gate implementation against spontaneous emission and technical imperfections.

C. Methods

In this subsection we elaborate on the numerical techniques developed and used for our simulation of the interacting two-atom system. First, we present methods to numerically estimate fidelity and time of a CZ_ϕ gate (2). Then we describe our strategy for designing a feasible CZ_ϕ gate based on the adiabatic-gate procedure (Sec. II B), and incorporating imperfections in this gate simulation (Sec. II C). Next, we provide a numerical recipe that redefines "efficiency" in the TQD technique (Sec. II D). Finally, we provide a method to compare adiabatic and cTQD CZ_ϕ gates in terms of their resource requirements.

We numerically evaluate the gate fidelity F_g and gate time T_g, and use these two quantities to assess the performance of a CZ_ϕ gate. F_g is estimated using Eq. (52), where $\rho(T_g)$ (51) is obtained by numerically integrating the GKSL equation (19) using the Python library `QuTiP`. T_g is the integration time and is related to the duration of a single pulse as $T_g = 4T$ for a cTQD CZ_ϕ gate, as compared to $T_g = 2T$ for an adiabatic CZ_ϕ gate. In addition to F_g and T_g, we analyze the trend in fidelity by estimating F_g for changing T_g values.

We prescribe simple numerical techniques to check feasibility and determine adiabaticity of a Rydberg-blockade CZ_ϕ gate. Our criterion for feasibility dictates that the intrinsic value of gate fidelity (52) should satisfy the condition

$$F_g^0 > \eta^e, \tag{54}$$

where threshold $\eta^{d\,(q)} = 0.9989\,(0.989)$. In the two-photon driving model, we lower the threshold by 1% because fidelity exceeding 0.99 requires numerically optimized pulses [26] rather than analytical pulses, which we use here for simplicity. For a two-level system initiating as an eigenstate $|E(t)\rangle$ (30) and evolving unitarily, we call the dynamics adiabatic if an instantaneous state $|\mathcal{I}(t)\rangle$ follows

$$|\langle E(t)|\mathcal{I}(t)\rangle|^2 \geqslant 0.99, \quad \forall t \in [0, T_g]. \tag{55}$$

Based on this condition, the CZ_ϕ gate is adiabatic if the dynamics within each two-dimensional subspace (43) is adiabatic.

In order to calculate values for pulse parameters that yields a feasible, adiabatic CZ_ϕ gate, we search over specified domains of these parameters. For LCG pulses (49), we choose

$$\begin{aligned} &0.1\ \mu s \leqslant T \leqslant 0.25\ \mu s, \quad 10\ \mathrm{MHz} \leqslant \Omega_0/2\pi \leqslant 25\ \mathrm{MHz}, \\ &20\ \mathrm{MHz} \leqslant \Delta_0/2\pi \leqslant 50\ \mathrm{MHz}, \quad 0.2T \leqslant \tau \leqslant 0.3T, \end{aligned} \tag{56}$$

and for ZCHG pulses (50), we consider

$$\begin{aligned} &50\ \mathrm{MHz} \leqslant \Omega_{B0}/2\pi, \quad \Omega_{R0}/2\pi \leqslant 300\ \mathrm{MHz}, \\ &100\ \mathrm{MHz} \leqslant \Delta_B/2\pi \leqslant 3000\ \mathrm{MHz}, \\ &0.1\ \mu s \leqslant T \leqslant 5\ \mu s,\ 0.25T \leqslant \tau_B, \tau_R \leqslant 0.35T. \end{aligned} \tag{57}$$

The values of these parameters are consistent with our previous work [26], and we have chosen parameter domains that are small enough to be numerically tractable but large enough to include feasible solutions. For each parameter tuple of LCG (ZCHG) pulse, we simulate the ARP CZ_π (STIRAP CZ) gate by unitary evolution of $H_B^d(t)$ $[H_B^q(t)]$ (12), with double-LCG (double-ZCHG) pulse functions as its coefficients, and calculate F_g^0. Using an in-house implementation of a global optimization algorithm called differential evolution (DE) [62], we then search over the parameter domains, which are not reused later, to find a tuple satisfying the feasibility condition (54).

We now provide a method for incorporating technical imperfections in our simulation of the adiabatic gates, and then define a nonadiabatic version of this adiabatic-gate procedure.

To account for technical imperfections, we modify the Hamiltonian coefficients by multiplying $p_\ell(\boldsymbol{r})$ (23) and f_ℓ (24) to the Rabi frequencies, and adding $\Delta_{\rm D}$ and $\Delta_{\rm m}$ (27) to the detuning terms. By introducing space dependence in the Hamiltonian $H_{\rm B}^{\rm e}(t)$, we now denote it by $H_{\rm B}^{\rm e}(t,\boldsymbol{r})$. In the nonadiabatic regime, the dynamics of $H_{\rm B}^{\rm d}(t,\boldsymbol{r})$ [$H_{\rm B}^{\rm q}(t,\boldsymbol{r})$] yields a nonadiabatic CZ$_\pi$ (CZ) gate, which we denote as a LCG CZ$_\pi$ (ZCHG CZ) gate.

For a transitionlessly driven two-level quantum system, the dynamics of $\check{H}^{\rm d}(t)$ (33) yields an efficient population transfer from an initial state $|1\rangle$ to the final state $|{\rm r}\rangle$ in any short time, given that there is no limit on the maximum laser intensity. To make $\check{H}^{\rm d}(t)$ practical, we redefine an "efficient" population transfer by imposing that the population of $|{\rm r}\rangle$ at the end of the dynamics exceeds 0.99 and the maximum value for $\Omega'(t)$ [(33b)] is within 10% of the maximum value for $\Omega(t)$ (8). This upper bound on $\Omega'(t)$ yields a lower limit on the pulse duration, which we denote as $T_{\rm min}$.

We investigate the interplay between two resources, namely maximum (real-valued) Rabi frequency $\Omega_{\rm max}$ and gate time $T_{\rm g}$, required for achieving high gate fidelity. To do this, we hypothesize functions relating these resources and empirically estimate the parameters of these functions. These parameters are then used for comparing different gate procedures. As a highly detuned two-photon driving is mathematically equivalent to a two-level system, we only compare between gates implemented using one-photon driving.

By numerically estimating the parameters of a power function (exponent, coefficient, and additive constant) that relates $\Omega_{\rm max}$ and $T_{\rm g}$ for a target fidelity, we determine the scaling of $\Omega_{\rm max}$ with decreasing $T_{\rm g}$. The value of $\Omega_{\rm max}$ is equal to Ω_0 (49) for the ARP CZ$_\pi$ gate, whereas $\Omega_{\rm max}$ is a function of Ω_0, Δ_0 and $T_{\rm g}$ for the cTQD CZ$_\phi$ gate and is numerically estimated in our simulation. For each $T_{\rm g}$, we fix values for other pulse parameters and search for the minimum $\Omega_{\rm max}$ required for achieving an ARP CZ$_\pi$ (cTQD CZ$_\phi$) with $F_{\rm g}^0 > 0.989$ ($F_{\rm g}^0 > 0.9989$). In terms of a unitless gate time $\bar{T}_{\rm g} := T_{\rm g}\ \mu{\rm s}^{-1}$, power parameter p, and constant frequencies ν_1 and ν_2, we hypothesize the relation between $\Omega_{\rm max}$ and $T_{\rm g}$ as a power function

$$\Omega_{\rm max} = \nu_1 \bar{T}_{\rm g}^{-p} + \nu_2, \tag{58}$$

in concordance with previous results [55]. The measure of goodness of fit for our simulation data to this power function is calculated using the R^2 score. We quantify and compare the performance of the two gates, namely, ARP CZ$_\pi$ and cTQD CZ$_\phi$, based on the estimate of p for each case.

We evaluate the speedup of a cTQD CZ$_\phi$ gate over an ARP CZ$_\pi$ gate, both yielding $F_{\rm g}^0 > 0.99$, for increasing values of $\Omega_{\rm max}$. Keeping $\Omega_{\rm max}$ almost same (within 10%) for both of these gates, we calculate speedup as the ratio of $T_{\rm g}$ for ARP and cTQD gates. Based on previous results [55], we expect the speedup value to saturate for both high and low magnitudes of $\Omega_{\rm max}$. Thus we can hypothesize the relation between a unitless maximum Rabi frequency $\bar{\Omega}_{\rm max} := {}^{\Omega_{\rm max}}/_{2\pi}\,{\rm MHz}^{-1}$ and speedup as a sigmoid function. To this end, we fit our simulation data to a generalized logistic function as

$$\frac{T_{\rm g}({\rm ARP})}{T_{\rm g}({\rm cTQD})} = \frac{a}{1+e^{-b\bar{\Omega}_{\rm max}+c}} + d, \tag{59}$$

for constants a, b, c, and d, and characterize the fit by calculating the R^2 score.

IV. RESULTS

In this section we present the results of our numerical analyses. In Sec. IV A (Sec. IV B), we begin by deriving generic expressions for the time-dependent coefficients of the cTQD Hamiltonian representing the one-photon (two-photon) excitation model. Using explicit analytical functions for these coefficients, we then simulate the operation of a cTQD CZ$_\phi$ gate and evaluate its fidelity. Moreover, we compare these gates against CZ$_\phi$ gates realized by employing typical pulse functions, i.e., LCG and ZCHG for one- and two-photon excitations, respectively. Finally, in Sec. IV C we compare resources required by a cTQD CZ$_\phi$ gate as compared to an adiabatic CZ$_\pi$ gate to achieve a target fidelity.

A. cTQD CZ$_\phi$ gate with one-photon excitation

The model for a pair of interacting atoms, where each atom is dipole-excited between states $|1\rangle$ and $|{\rm r}\rangle$, is mathematically described by the cTQD Hamiltonian $\tilde{H}_{\rm B}^{\rm d}(t)$ (41). We derive generic expressions for the time-dependent coefficients of this Hamiltonian from the adiabatic Hamiltonian $H_{\rm B}^{\rm d}(t)$ (12).

We first derive the TQD Hamiltonian $\check{H}_{\rm B,eff}^{\rm d}(t)$ acting on the two-dimensional subspace $\mathscr{H}_{\rm rr}$ (43). For an effective Rabi frequency $\Omega_{\rm eff}^{\rm d} := \sqrt{2}\Omega$ and an effective detuning $\Delta_{\rm eff}^{\rm d} := \Delta$, the adiabatic Hamiltonian acting on $\mathscr{H}_{\rm rr}$ is

$$\begin{aligned} H_{\rm B,eff}^{\rm d}(t) = {}& \frac{\Omega_{\rm eff}^{\rm d}}{2}[|11\rangle\langle +| + |+\rangle\langle 11|] \\ & + \frac{\Delta_{\rm eff}^{\rm d}}{2}[-|11\rangle\langle 11| + |+\rangle\langle +|]. \end{aligned} \tag{60}$$

Using the TQD technique (Sec. II D), we calculate the coefficients for the two-level control Hamiltonian (32) as

$$\Omega_{\rm c}^{\rm d} := \frac{\Omega_{\rm eff}^{\rm d}\dot{\Delta}_{\rm eff}^{\rm d} - \Delta_{\rm eff}^{\rm d}\dot{\Omega}_{\rm eff}^{\rm d}}{\left(\Delta_{\rm eff}^{\rm d}\right)^2 + \left(\Omega_{\rm eff}^{\rm d}\right)^2}, \quad \theta^{\rm d} := \tan^{-1}\frac{\Omega_{\rm c}^{\rm d}}{\Omega_{\rm eff}^{\rm d}}. \tag{61}$$

The TQD Hamiltonian for $\mathscr{H}_{\rm rr}$ is then calculated as

$$\begin{aligned} \check{H}_{\rm B,eff}^{\rm d}(t) = {}& \frac{\sqrt{\left(\Omega_{\rm eff}^{\rm d}\right)^2 + \left(\Omega_{\rm c}^{\rm d}\right)^2}}{2}[|11\rangle\langle +| + |+\rangle\langle 11|] \\ & + \frac{\Delta_{\rm eff}^{\rm d} + \dot{\theta}^{\rm d}}{2}[-|11\rangle\langle 11| + |+\rangle\langle +|], \end{aligned} \tag{62}$$

whose dynamics effects an efficient population transfer between $|11\rangle$ and $|+\rangle$ over any integration time.

From $\check{H}_{\rm B,eff}^{\rm d}(t)$, we now derive generic expressions for the time-dependent coefficients of $\tilde{H}_{\rm B}^{\rm d}(t)$. This is done by first obtaining $\tilde{H}_{\rm B,eff}^{\rm d}(t)$ from $\check{H}_{\rm B,eff}^{\rm d}(t)$ (47) and then performing an inversion operation on $\tilde{H}_{\rm B,eff}^{\rm d}(t)$ (48). These operations yield the time-dependent Rabi frequency

$$\begin{aligned} \tilde{\Omega}(t) &= \sqrt{\frac{\left(\Omega_{\rm eff}^{\rm d}\right)^2 + \left(\Omega_{\rm c}^{\rm d}\right)^2}{2}} \\ &= \sqrt{\Omega^2(t) + \left(\frac{\Omega(t)\dot{\Delta}(t) - \Delta(t)\dot{\Omega}(t)}{\Delta^2(t) + 2\Omega^2(t)}\right)^2}, \end{aligned} \tag{63}$$

and detuning

$$\tilde{\Delta}(t) = \Delta_{\rm eff}^{\rm d} + \dot{\theta}^{\rm d} = \Delta + \dot{\theta}^{\rm d} \tag{64}$$

for the laser pulse in Fig. 1(a). Using the above expressions for Rabi frequency and detuning in Eq. (39), we finally derive $\tilde{H}_{\rm B}^{\rm d}(t)$ for the two-atom system.

Having derived generic expressions for Hamiltonian coefficients, we now present numerical results on the Hamiltonian dynamics and on our fast, high-fidelity cTQD CZ_ϕ gate. In the following, we state the feasible parameters for LCG pulses, compare population dynamics achieved by these pulses and their corresponding TQD pulses, and compute the pulse sequence for yielding a high-fidelity gate.

We calculate explicit expressions for the TQD pulse functions $\tilde{\Omega}^+(t)$ and $\tilde{\Delta}^+(t)$ by choosing $\Omega(t)$ and $\Delta(t)$ of the LCG form (49) with feasible parameters. Using DE, we estimate feasible parameters for an adiabatic LCG pulse, of duration $T = 0.24$ μs, as

$$\Omega_0/2\pi = 24.92 \text{ MHz}, \ \tau = 0.266T, \ \Delta_0/2\pi = 49.55 \text{ MHz}. \tag{65}$$

Numerical simulation of the CZ_π gate with a double-adiabatic sequence of LCG pulses yields $F_{\rm g}^0 = 0.999$ and $T_{\rm g} = 0.48$ μs. We empirically establish that $T_{\rm g} = 0.48$ μs is the minimum time for which the pulse sequence is adiabatic for the above choice of parameters and also delivers a feasible fidelity (54).

We now compare a LCG pulse against the corresponding TQD pulse, when both of these pulses are applied for one-quarter of the adiabatic LCG pulse duration, 0.24 μs. In Fig. 3(a) we plot $\Omega(t)$ and $\Delta(t)$ corresponding to the LCG pulse of duration $T = 0.06$ μs and predetermined parameters (65). Whereas for the TQD pulse, $\tilde{\Omega}^+(t)$ has a fatter tail as compared to a Gaussian function and $\tilde{\Delta}^+(t)$ is nonlinear in time. Furthermore, we numerically evaluate the ratio of the two pulse energies to be near unity. In Fig. 3(b) we investigate the unitary dynamics of $H_{\rm B}^{\rm d}(t)$ [$\tilde{H}_{\rm B}^{\rm d}(t)$], without any parameter fluctuations, for a LCG (TQD) pulse and an initial atomic state $|11\rangle$. With the LCG pulse, the population P_+ of the entangled state reaches 0.75 in time $T/2$ and changes very little, up to small oscillations, until the end of the pulse duration. On the other hand, using the TQD pulse, P_+ increasing smoothly from 0 to 1 over time T and reaches $\approx$1 at $t \approx .05$ μs.

To implement a high-fidelity cTQD CZ_ϕ gate in half the gate time as compared to the adiabatic CZ_π gate, we design $\tilde{\Omega}(t)$ as a sequence of phase-shifted $\tilde{\Omega}^+(t)$ and $\tilde{\Delta}(t)$ as a sequence of $\tilde{\Delta}^+(t)$; see Fig. 4(a). Based on the unitary dynamics of $\tilde{H}_{\rm B}^{\rm d}(t)$, we observe in Fig. 4(b) that the populations of the initial states $|10\rangle$ and $|11\rangle$ return efficiently back to the respective states at the end of the pulse sequence. Moreover, the phase difference $\phi_{11} - 2\phi_{10}$, after a few oscillations between $-\pi$ and π, eventually saturates at $-\pi$. Thus upon executing efficient population transfers and satisfying the phase relation (42), our gate procedure delivers $F_{\rm g}^0 = 0.999$ over $T_{\rm g} = 0.24$ μs, making our cTQD CZ_ϕ gate twice as fast as the adiabatic CZ_π gate.

Now we investigate the variation of gate infidelity $1 - F_{\rm g}$ (both intrinsic and realistic) with changing gate time for two types of Rydberg-blockade gates, namely cTQD CZ_ϕ gate and LCG CZ_π gate [Fig. 5(a)]. In these simulations, we use the predetermined values (65) for LCG parameters and consider spontaneous emission, nonzero atomic temperature, finite beam waist and fluctuations in magnetic field and laser intensity. The upper bound for $T_{\rm g}$ in Fig. 5(a) is equal to the time for the adiabatic gate with LCG pulses, which is 0.48 μs. The lower bound is $4T_{\rm min}$, where $T_{\rm min} = 0.03$ μs for the TQD pulse obtained using the above LCG parameters. Our cTQD CZ_ϕ gate delivers $F_{\rm g}^0 > 0.99$ and $F_{\rm g} > 0.988$ for all $T_{\rm g}$ between these two bounds, whereas both $F_{\rm g}^0$ and $F_{\rm g}$ for the LCG CZ_π gate start to fall significantly when reducing $T_{\rm g}$ below 0.3 μs. Moreover, the cTQD gate fidelities have much smaller standard errors than the LCG gate fidelities for lower $T_{\rm g}$, whereas these errors are almost comparable for higher $T_{\rm g}$, as seen in Fig. 5(b).

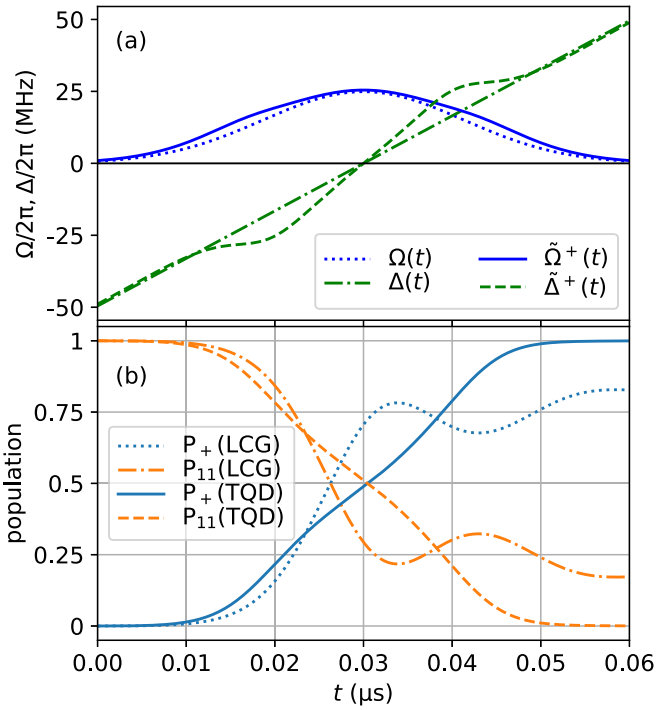

FIG. 3. Pulse functions and population dynamics over duration $T = 0.06$ μs for LCG and its corresponding TQD pulses. Other parameters are fixed as in Eq. (65). (a) Solid blue (dashed green) line for TQD pulse function $\tilde{\Omega}^+(t)$ [$\tilde{\Delta}^+(t)$] and dotted blue (dash-dotted green) line for LCG pulse function $\Omega(t)$ [$\Delta(t)$]. (b) Solid (dotted) azure and dashed (dash-dotted) orange lines denote the time-dependent populations of the states $|+\rangle$ and $|11\rangle$, respectively, corresponding to the TQD (LCG) pulse.

B. cTQD CZ_ϕ gate with two-photon excitation

Here we provide results for our cTQD CZ_ϕ gate implementation using two-photon driving of two atoms. First, we derive expressions for the time-dependent coefficients of the cTQD Hamiltonian $\tilde{H}_{\rm B}^{\rm q}(t)$ (41). Next, we design a pulse sequence that yields a high-fidelity cTQD CZ_ϕ gate, which is twice as fast as the adiabatic CZ gate. Finally, we show how fidelity changes with decreasing gate time in the presence and absence of imperfections and decay.

We derive an effective two-level adiabatic Hamiltonian, followed by an effective TQD Hamiltonian, with both acting on the subspace $\mathscr{H}_{\rm rr}$ (43). Adiabatic elimination of state $|\mathrm{p}\rangle$

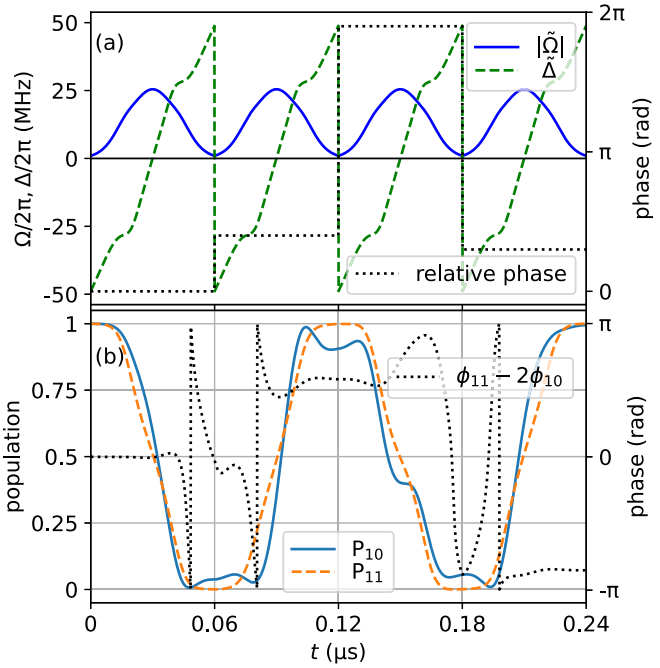

FIG. 4. Pulse functions, population dynamics and phase-difference dynamics over $T_g = 0.24$ μs for implementing a cTQD CZ_ϕ gate based on the one-photon transition model. (a) $\tilde{\Omega}(t)$ is a sequence of four (two pairs) time-translated $\tilde{\Omega}^+(t)$ [Fig. 3(a)], with a relative phase shift of $\phi_r/\pi = 0.4$ between the pulses in each pair and a phase shift of $\phi_R/\pi = 1.9$ between the two pairs, and $\tilde{\Delta}(t)$ is a sequence of four time-translated $\tilde{\Delta}^+(t)$ [Fig. 3(a)]. (b) P_{10} (P_{11}) is the time-dependent population of the state $|10\rangle$ ($|11\rangle$) as shown by solid azure (dashed orange) line, and the dotted line shows the time-dependent phase difference $\phi_{11} - 2\phi_{10}$.

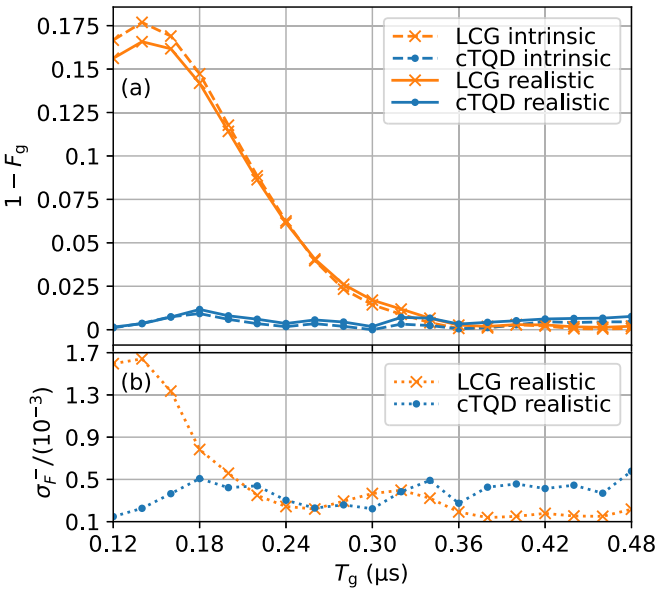

FIG. 5. Gate infidelity ($1 - F_g$) and standard error of fidelity (σ_F^-) over $T_g \in [0.12\ \mu s, 0.48\ \mu s]$ for LCG CZ_π gate and cTQD CZ_ϕ gate, implemented using the one-photon transition model. We show the simulation results by markers (cross or circle) and connect them with lines (solid, dashed, or dotted). (a) Dashed (solid) orange line, with cross markers, denotes intrinsic (realistic) infidelity for LCG CZ_π gate. Dashed (solid) azure line, with circle markers, denotes intrinsic (realistic) infidelity for cTQD CZ_ϕ gate. Each point on solid lines represents the mean infidelity calculated for 100 random instances of master-equation evolution. (b) Each point, marked by a cross (circle) for LCG CZ_π (cTQD CZ_ϕ) gate, on the dotted lines represent σ_F^- calculated for these 100 fidelity estimates.

from both atoms yields a block-diagonal Hamiltonian. After eliminating $|rr\rangle$ according to the Rydberg-blockade condition (13), one of these blocks has support on only $\mathscr{H}_{rr}$. This two-dimensional Hamiltonian $H^q_{B,eff}(t)$ is of the same form as the effective Hamiltonian (60), with the corresponding time-dependent coefficients being

$$\Omega^q_{eff} := -\sqrt{2}\frac{\Omega_B\Omega_R}{2\Delta_B}, \quad \Delta^q_{eff} := \frac{\Omega_B^2 - \Omega_R^2}{4\Delta_B}. \tag{66}$$

Using the TQD technique on $H^q_{B,eff}(t)$, we then construct the control terms Ω^q_c and θ^q, which are similar to Eq. (61). Finally, we derive the effective TQD Hamiltonian

$$\check{H}^q_{B,eff}(t) = \frac{\tilde{\Omega}^q_{eff}}{2}[|11\rangle\langle+| + |+\rangle\langle 11|] + \frac{\tilde{\Delta}^q_{eff}}{2}[-|11\rangle\langle 11| + |+\rangle\langle+|], \tag{67}$$

where the time-dependent coefficients are

$$\tilde{\Omega}^q_{eff} := \sqrt{\left(\Omega^q_{eff}\right)^2 + \left(\Omega^q_c\right)^2}, \quad \tilde{\Delta}^q_{eff} := \Delta^q_{eff} + \dot{\theta}^q. \tag{68}$$

$H^q_{B,eff}(t)$ drives an efficient $|11\rangle \leftrightarrow |+\rangle$ transition in the adiabatic regime, whereas $\check{H}^q_{B,eff}(t)$ renders this transition faster.

From $\check{H}^q_{B,eff}(t)$, we now derive expressions for the time-dependent coefficients of $\tilde{H}^q_B(t)$. Operating under the adiabatic-elimination condition (10), we require a constant detuning

$$\tilde{\Delta}_B(t) \equiv \Delta_B. \tag{69}$$

Proceeding similarly to the one-photon case, we first assign functions to the effective Hamiltonian $\tilde{H}^q_{B,eff}(t)$ according to Eq. (47). Then we invert this equation, according to Eq. (48), to obtain time-dependent expressions for Rabi frequencies, namely,

$$\tilde{\Omega}_B(t) = \sqrt{2\Delta_B\left[\sqrt{\left(\tilde{\Delta}^q_{eff}\right)^2 + \left(\tilde{\Omega}^q_{eff}/\sqrt{2}\right)^2} + \tilde{\Delta}^q_{eff}\right]},$$
$$\tilde{\Omega}_R(t) = \sqrt{2\Delta_B\left[\sqrt{\left(\tilde{\Delta}^q_{eff}\right)^2 + \left(\tilde{\Omega}^q_{eff}/\sqrt{2}\right)^2} - \tilde{\Delta}^q_{eff}\right]}, \tag{70}$$

corresponding to the blue- and red-detuned lasers, respectively, in Fig. 1(b). These expressions (69) and (70) then establish $\tilde{H}^q_B(t)$.

We estimate parameters for the adiabatic ZCHG pulses (50) delivering a feasible (54) CZ gate. For a pair of ZCHG pulses effecting STIRAP over $T = 0.81$ μs, DE yields the following feasible values for pulse parameters:

$$\Omega_{B0}/2\pi = 300\ \text{MHz}, \quad \Omega_{R0}/2\pi = 300\ \text{MHz}$$
$$\Delta_B/2\pi = 1762.90\ \text{MHz}, \quad \tau_B = \tau_R = 0.35T. \tag{71}$$

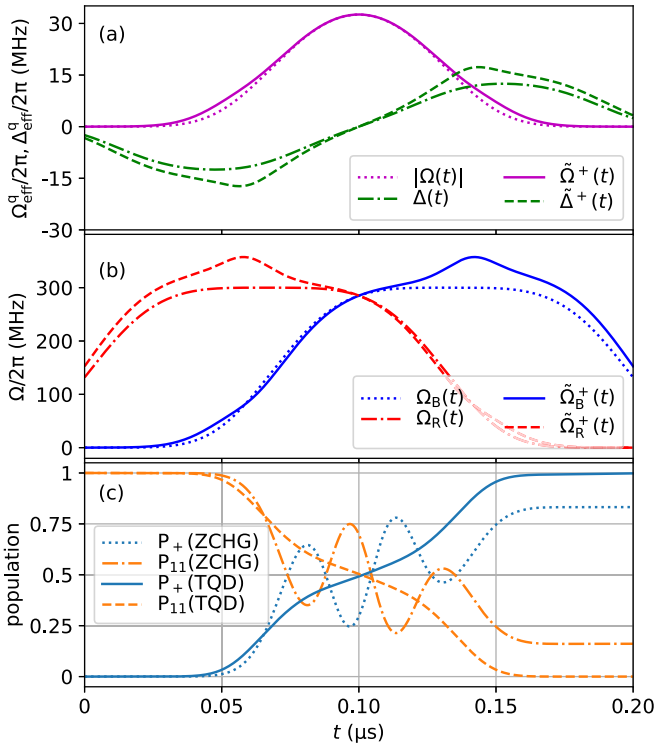

FIG. 6. Pulse functions and population dynamics over duration $T = 0.2$ μs for ZCHG and the corresponding TQD pulses. Other parameters are fixed as in Eq. (71). (a) Effective Rabi frequency and detuning for the pair of TQD (ZCHG) pulses shown by solid (dotted) magenta and dashed (dash-dotted) green lines, respectively. For simplicity, we omit subscript "eff" and superscript "q" in the legend. (b) Solid (dotted) blue and dashed (dash-dotted) red lines represent the pair of Rabi frequencies for TQD (ZCHG) pulses. (c) Solid (dotted) azure and dashed (dash-dotted) orange lines denote the time-dependent populations of $|+\rangle$ and $|11\rangle$, respectively, corresponding to the TQD (ZCHG) pulses.

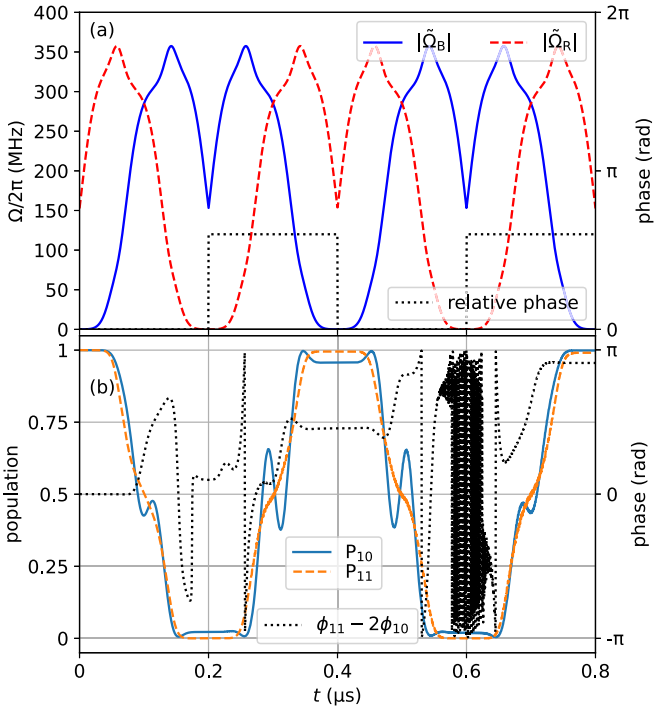

FIG. 7. Pulse functions, population dynamics and phase-difference dynamics over $T_g = 0.8$ μs for implementing a cTQD CZ_ϕ gate based on the two-photon transition model. (a) $\tilde{\Omega}_{B,R}$ is a sequence of four (two pairs) time-translated $\tilde{\Omega}^+_{B,R}(t)$ [Fig. 6(b)], with a relative phase shift of $\phi_r/\pi = 0.6$ between the pulses in each pair and a phase shift of $\phi_R/\pi = 0$ between the two pairs, and $\tilde{\Delta}_B/2\pi = 1762.90$ MHz. (b) P_{10} (P_{11}) is the time-dependent population of the state $|10\rangle$ ($|11\rangle$) as shown by solid azure (dashed orange) line, and the dotted line shows the time-dependent phase difference $\phi_{11} - 2\phi_{10}$.

Using a sequence of two STIRAP pulses, with the above parameters, we achieve a CZ gate with $F_g = 0.996$ and $T_g = 1.62$ μs in our simulation. We numerically demonstrate that these pulses adiabatically drive the $|1\rangle \leftrightarrow |r\rangle$ transition for each atom, without significantly populating the state $|p\rangle$. By eliminating $|p\rangle$, this transition is now an effective two-level transition. Furthermore, we numerically establish that $T_g = 1.62$ μs is the minimum time for which the pulses are adiabatic for the above choice of parameters.

Now we compare nonadiabatic driving by ZCHG pulses against transitionless quantum driving of the $|11\rangle \leftrightarrow |+\rangle$ transition over an integration time of 0.2 μs, which is one-quarter of the total duration for the above pair of feasible adiabatic pulses. In Fig. 6(a) we observe that the effective Rabi frequency and detuning (66) for the pair of ZCHG pulses resembles Gaussian and sinusoidal functions, respectively. The TQD technique flattens the tail of the effective Rabi frequency and add nonlinear modulation to the effective detuning. The Rabi frequencies for the TQD pulses are nearly hyper-Gaussians with a sharper and little asymmetric tip as compared to the flat top ZCHG pulses, as seen in Fig. 6(b). Although the peak Rabi frequencies for the two TQD pulses are significantly higher than those for their corresponding ZCHG pulses, the effective functions are almost equal. From Fig. 6(c), we notice that the TQD pulses result in near-unity population transfer, i.e., $P_+ \approx 1$, at $t \approx 0.16$, as compared to the 80% saturation level using ZCHG pulses.

Using the pair of TQD pulses, we now construct a pulse sequence yielding a high-fidelity cTQD CZ_ϕ gate, which is twice as fast as the adiabatic CZ gate. To this end, the coefficients in $\tilde{H}^q_B(t)$ are designed as piecewise-smooth functions, particularly $\tilde{\Omega}_B(t)$ and $\tilde{\Omega}_R(t)$ are sequences of phase-shifted TQD pulses [Fig. 7(a)], and $\tilde{\Delta}_B(t)$ is constant over the gate time. The one (two) cusp(s) in the red-detuned (blue-detuned) pulse of Fig. 7(a) are artifacts of this pulse construction being piecewise continuous. Our estimates for relative phases ensure that the population, governed by unitary dynamics of $\tilde{H}^q_B(t)$, of each basis state efficiently return back to itself after time $T_g = 0.8$ μs; see Fig. 7(b). We note that the cusps in Fig. 7(a) do not manifest as discontinuities in the functions or derivatives thereof in Fig. 7(b). Moreover, the relation (42) between phases of basis states holds, as evident from the convergence of phase difference to 0.909π at T_g, with high oscillations centered around $t = 0.6$ μs. Consequent to the pulses satisfying the population dynamics and phase relation (C1–C3), our predicted gate fidelity is 0.987 over a gate time of 0.8 μs, making our gate procedure twice faster with a slight decrease in the fidelity.

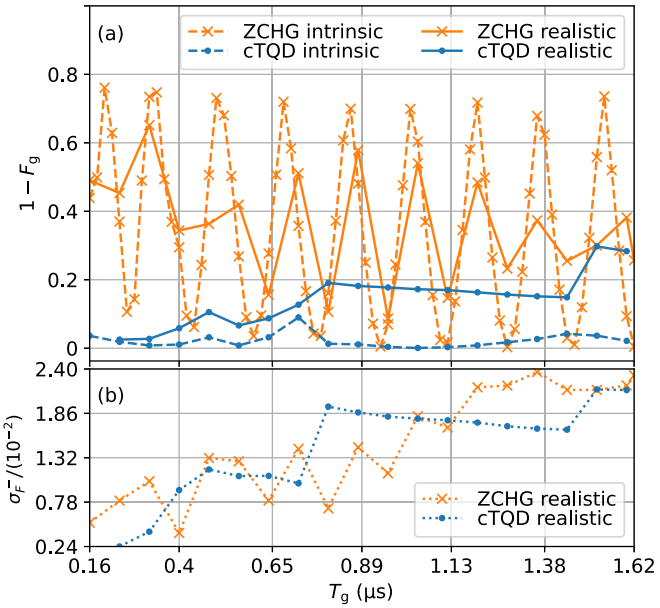

FIG. 8. Gate infidelity $(1 - F_g)$ and standard error of fidelity (σ_F^-) over $T_g \in [0.16\ \mu s, 1.62\ \mu s]$ for ZCHG CZ gate and cTQD CZ_ϕ gate, implemented using the two-photon transition model. We show the simulation results by markers (cross or circle) and connect them with lines (solid, dashed, or dotted). (a) Dashed (solid) orange line, with cross markers, denotes intrinsic (realistic) infidelity for ZCHG CZ gate. Dashed (solid) azure line, with circle markers, denotes intrinsic (realistic) infidelity for cTQD CZ_ϕ gate. Each point on the solid lines represents the mean infidelity calculated for 100 random instances of master-equation evolution. (b) Each point, marked by cross (circle) for ZCHG CZ (cTQD CZ_ϕ) gate, on the dotted lines represent σ_F^- calculated for these 100 fidelity estimates.

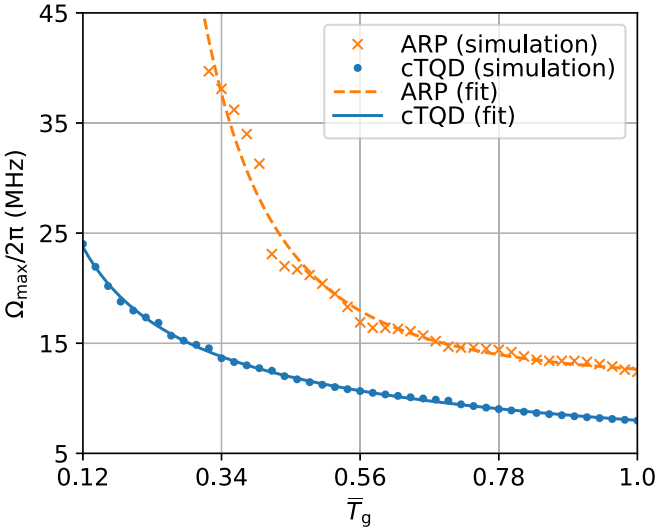

FIG. 9. Isofidelity plots to show scaling of the maximum (real-valued) Rabi frequency Ω_{max} with respect to the unitless gate time $\bar{T}_g$. Isofidelity plot for the ARP CZ_π gate corresponds to $F_g^0 > 0.989$, whereas for the cTQD CZ_ϕ gate, implemented using the one-photon transition model, $F_g^0 > 0.9989$. Other parameters are $\Delta_0/2\pi = 49.55$ MHz, $\tau/T = 0.266$ and $B/2\pi = 3$ GHz. Simulation results, denoted by orange cross (azure circle) markers, for the ARP CZ_π (cTQD CZ_ϕ) gate are fitted to the power function (58), with $\nu_1/2\pi = 1.34 \pm 0.33\ (7.18 \pm 0.38)$ MHz, $\nu_2/2\pi = 11.31 \pm 0.66\ (0.82 \pm 0.41)$ MHz and $p = 2.76 \pm 0.22\ (0.55 \pm 0.02)$, shown as the dashed orange (solid azure) line.

We now compute fidelities for our cTQD CZ_ϕ gate in the presence of spontaneous emission and technical imperfections, and compare with ZCHG gate for changing gate times, see Fig. 8. The fidelities for both intrinsic and realistic ZCHG gates oscillate rapidly with T_g, where the trough values for intrinsic fidelity gradually decrease with increasing T_g. In the presence of noise, fidelities drop for both higher and lower T_g, with σ_F^- being $10\times$ higher in higher end of T_g as compared to the lower values. On the other hand, cTQD gate yields $F_g^0 > 0.96$ over the whole range of T_g, with very small oscillations. Adding noise to this gate yields lower fidelities for high T_g, but the effect of noise is low for small T_g. The best estimate of fidelity is 0.975 at $T_g = 0.24$ μs.

C. Resource requirement for cTQD CZ_ϕ gate

We empirically calculate resources required for implementing high-fidelity CZ_ϕ gates by unitary evolution of adiabatic and cTQD Hamiltonians with one-photon driving, and present these results here. First, we evaluate the scaling of Ω_{max} with decreasing T_g for our cTQD CZ_ϕ gate and compare this scaling against the scaling obtained for the ARP CZ_π gate. Next, we show how much faster the cTQD gate is over ARP gate for changing values of Ω_{max}. Finally, we provide a mathematical model describing the relation between speedup values and Ω_{max} for our simulation data.

In Fig. 9 we show isofidelity plots for determining the scaling of Ω_{max} with decreasing T_g. We vary T_g between 0.12 μs and 1.0 μs, i.e., $\bar{T}_g \in [0.12, 1.0]$, to allow for an order-of-magnitude change in gate time. For $T_g < 0.32$ μs, ARP fails to deliver a CZ_π gate with the target fidelity of 0.989. The adiabatic-gate procedure exhibits a sharp fall in the required Ω_{max} between gate times of 0.40 μs and 0.42 μs, whereas Ω_{max} for our cTQD CZ_ϕ gate smoothly reduces over the whole range of T_g. By fitting each of these two isofidelity plots to our assumed power function (58), we evaluate R^2 scores of 0.97 and 0.99 corresponding to the ARP and cTQD gates, respectively.

We now plot the variation of speedup with $\bar{\Omega}_{max}$ in Fig. 10. Based on our results in Fig. 9, we vary $\Omega_{max}/2\pi$ between 10 MHz and 40 MHz, which translates to $\bar{\Omega}_{max} \in [10, 40]$. We observe that the magnitudes for speedup saturate around 2.3 and 4.7 for lower and higher Ω_{max}s, respectively. These values match the parameters of the fitted logistic model (59). Between $\bar{\Omega}_{max}$ values of 20 and 30, we notice a rapid increase in speedup. Additionally, fitting out simulation data to the logistic model yields a R^2 score of 0.96.

V. DISCUSSION

We aim to design laser-pulse functions that deliver high-fidelity, fast CZ gates for neutral atom quantum computing. Our model includes major technical imperfections for a system of two Cs atoms simultaneously driven, either by an one-photon process or a two-photon process, between their ground and highly excited Rydberg levels using off-resonant

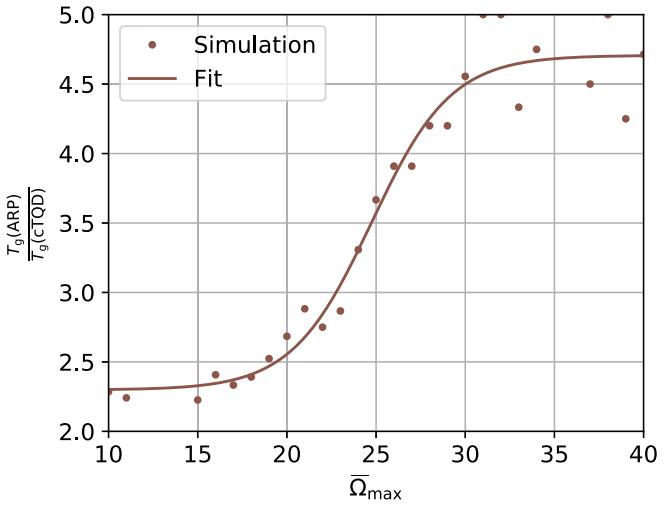

FIG. 10. Trend in speedup $\frac{T_g(\mathrm{ARP})}{T_g(\mathrm{cTQD})}$ with increasing values of the unitless maximum Rabi frequency $\bar{\Omega}_{\max}$, for fixed $\Delta_0/2\pi =$ 49.55 MHz, $\tau/T = 0.266$ and $B/2\pi = 3$ GHz. Isofidelity plot corresponds to $F_g^0 > 0.99$ for both ARP CZ_π and cTQD CZ_ϕ gates. Simulation results (circles) are fitted to the logistic function (59) (solid line) with parameters $a = 2.41 \pm 0.15$, $b = 0.45 \pm 0.08$, $c = 11.09 \pm 2.05$, and $d = 2.29 \pm 0.1$.

and broadband lasers. The pair of Rydberg atoms experiences a strong dipole-dipole interaction, which results in a controlled-phase gate on the atomic qubits over a time T_g. We design these Rydberg-excitation pulses as sequences of time-dependent functions, whose expressions are derived by applying our modified TQD technique. Using our pulse sequences and including spontaneous emission and technical imperfections, we show that numerical integration of the master equation predicts high-fidelity CZ gates for Cs atoms.

We adapt the standard TQD technique for the interacting two-atom system, which is mathematically represented by a Hamiltonian acting on a 25-dimensional Hilbert space. As this high-dimensional space can be decomposed into a direct sum of one- and two-dimensional subspaces under suitable approximations, we can apply the standard TQD technique independently to the Hamiltonians acting on these subspaces. This direct application of the TQD technique results in an infeasible Hamiltonian. Our modified TQD technique involves projecting the high-dimensional adiabatic Hamiltonian to one relevant two-dimensional subspace, applying TQD to the effective Hamiltonian of this subspace and finally lifting this TQD Hamiltonian back to a 25×25 nonadiabatic Hamiltonian called the cTQD Hamiltonian, which is a valid representation of our model. Using this technique, we derive amplitude [(63) and (70)] and frequency [(64) and (69)] modulations for the adiabatic pulses that leads to high-fidelity gates over shorter gate times.

We revisit the double-pulse adiabatic-gate procedure [26] as we need an adiabatic Hamiltonian as a starting point for constructing our cTQD Hamiltonian. To obtain expression for this initial Hamiltonian, we describe the adiabatic transitions between ground and Rydberg levels using a LCG pulse (49) for the one-photon model and a pair of ZCHG pulses (50) for the two-photon model. A global search over LCG (ZCHG) pulse parameters yields a CZ_π (CZ) gate with intrinsic fidelity $F_g^0 = 0.999\,(0.996)$. Although the individual Rabi frequencies are high for the two-photon transition, the effective Rabi frequency is similar to the one-photon case, as evident from Fig. 6(a). Moreover, the gate implemented by the single-photon transition is three times as fast as the one implemented by the two-photon transition because STIRAP is inherently slower than ARP.

Using the above LCG and ZCHG pulses, we derive time-dependent TQD pulses for one- and two-photon driving, respectively. In Fig. 3 we observe that redistributing energy over pulse duration enables the system to reach the final state more rapidly than the linear sweep. Intuitively, the modulation in detuning effectively cancels outs some frequency components, making the pulse narrowband and the transition more efficient. This analysis agree with that of Malossi *et al.* [63], where they investigate population-transfer efficiencies for various pulse shapes, as opposed to reverse-engineering pulses using TQD. For the two-photon transition, pulse modulation by the TQD technique has the same effect on the population dynamics (Fig. 6). On the other hand, the LCG (ZCHG) pulse is nonadiabatic over 0.06 μs (0.2 μs), thus yielding an inefficient population transfer to the final state. The oscillations in these time-dependent populations are due to transitions between the instantaneous eigenstates.

By concatenating phase-shifted, time-translated TQD pulses, we design piecewise-smooth pulse functions that result in high-fidelity CZ_ϕ gates at nonadiabatic T_g. In Figs. 4(a) and 7(a), discontinuities occurring at multiples of $T_g/4$ are artifacts of this pulse-shaping method and can be smoothed out by using analytical functions [26]. Unitary evolution generated by our cTQD Hamiltonian results in the desired population and phase dynamics, as evident from Figs. 4(b) and 7(b), consequently achieving high-fidelity gates. As the cusps in the pulse functions do not deleteriously affect the population and phase dynamics, we do not expect smoothing the pulse shapes to drastically impact gate fidelity. The second pair of phase-shifted pulses aid in compensating for the loss in population of $|10\rangle$ over $T_g/2$, thus further validating our pulse design procedure. As the phase difference is approximately $\pi/2$ at $T_g/2$, a gate equivalent to $\sqrt{\mathrm{CZ}}$ is created. The sudden jumps in the plot for phase difference are artifacts of numerical instabilities, which can be removed by plotting with a larger time step.

We numerically investigate how F_g^0 changes with changing T_g, but keeping the maximum Rabi frequency almost constant (within 10%). Intuitively, we expect a steady increase in F_g^0 with increasing T_g [Fig. 5(a)], but our simulation results for the ZCHG CZ gate show an oscillating F_g^0 in Fig. 8(a). This qualitatively different behavior of fidelity is not due to spontaneous emission from the extra level $|p\rangle$ involved in the two-photon case because F_g^0 is the noiseless fidelity. The origin of this oscillation in fidelity is the oscillation in ϕ_{11}, with both having nearly similar frequencies of 6.25 MHZ and 8 MHz, respectively. For our choice of STIRAP pulse shapes, the relevant time-dependent eigenenergy of $H_B^q(t)$ is symmetric about $T_g/2$, as is also seen in Ref. [33]. This results in an overall time-dependent ϕ_{11}, which oscillates between $\pm\pi$. The energy of the effective pulse (66) contributes to the value and, consequently, to the time dependence of ϕ_{11}; thus

TABLE II. Comparing different gate procedures. $F_g^{(s)}$ is the fidelity in the presence of spontaneous emission from excited levels.

Procedure	Excitation	Implementation	Time (μs)	F_g^0	$F_g^{(s)}$	F_g	Area/2π
Standard	Two-photon	Experiment [32]	1.12	—	—	0.89	—
Simultaneous	Two-photon	Experiment [11]	0.8	—	—	0.955	—
Adiabatic	One-photon	Simulation [26]	0.54	—	0.999	—	—
Adiabatic	Two-photon	Simulation [26]	1	—	0.997	—	—
cTQD	One-photon	Simulation	0.12	0.9989	0.9988	0.9985	4.6
cTQD	Two-photon	Simulation	0.24	0.981	0.978	0.975	4.92
Adiabatic	One-photon	Simulation	0.48	0.9993	0.9990	0.9980	14.86
Adiabatic	Two-photon	Simulation	1.62	0.996	0.986	0.743	21.75

fixing this energy for decreasing T_g is one way to remove the oscillations in F_g^0. On the other hand, our cTQD CZ_ϕ gate yields smaller fluctuations in F_g^0 due to our feasible choices for parameters ϕ_r and ϕ_R.

Similar to F_g^0, the realistic fidelity F_g also oscillates with T_g. Moreover, F_g for the ZCHG gate drops for higher T_g [Fig. 8(a)], as compared to F_g for the LCG gate that keeps increasing [Fig. 5(a)]. The adiabatic ZCHG gate is about four times slower than the adiabatic LCG gate, thus suffers from more noise as also evident from Figs. 5(b) and 8(b). Our cTQD CZ_ϕ gate beats the LCG (ZCHG) gate at lower values for T_g, yielding the best performance of $F_g = 0.9985\,(0.975)$ at $T_g = 0.12\,(0.24)$ μs. Whereas in the adiabatic limit, both gates perform equivalently in terms of fidelity and sensitivity to noise.

We summarize performances of our cTQD CZ_ϕ gates, relevant experimental gates [11,32] and simulated adiabatic gates [26] in Table II. For a reasonable comparison, we only discuss experiments that use Cs atomic qubits. Gates based on one-photon excitation of Rydberg atoms, although experimentally challenging, yield highest fidelities over shortest times. Spontaneous emission from excited levels reduce fidelity significantly for gates implemented based on two-photon transition. Our procedure, with the two-photon-driving model, generates a Bell state with 50% less infidelity than that for the state-of-the-art implementation over one-quarter gate time. For a detailed comparison with the adiabatic-gate procedure [26], we report results from our simulations of adiabatic gates. Comparing these values against cTQD gate fidelities, we infer that our procedure succeeds in making the adiabatic gates faster, but keeping F_g^0 same.

We compare the adiabatic and cTQD CZ_ϕ gates based on their resource requirements for preparing high-fidelity Bell states. For simplicity, and making the reasonable approximation of a high-detuned two-photon transition, we restrict our attention to the one-photon-transition model for Rydberg excitation. Our simulation data closely align our assumed functions relating Ω_{max} and T_g, as evident from their high (>0.95) R^2 values; see Figs. 9 and 10. Fixing a target fidelity, both adiabatic and cTQD gates can be sped up by increasing Ω_{max}, but the rate of increase is different. From Fig. 9 we infer that the required Ω_{max} for the ARP gate increases five times faster than that for the cTQD gate, when we decrease T_g from 1 μs to 0.12 μs. Moreover, the power factor p (58) satisfies the inequality (6) for the adiabatic passage, whereas the cTQD gate saturates the lower bound for this inequality by employing TQD. In Fig. 10 we notice that for a fixed value of Ω_{max}, the cTQD gate is at least twice as fast compared to its adiabatic counterpart, but this speedup rapidly increases and eventually saturates at higher values of Ω_{max}. Moreover, these two plots are interrelated, i.e., one can be explained from the other.

VI. CONCLUSIONS

Quantum computing with neutral atoms is a promising direction towards quantum advantage, with recent demonstrations of quantum algorithms [11,64], error-correcting codes [65], and analog simulations [17,18]. This platform bears an inherent advantage due to its unique ability to coherently control several stable qubits with the possibility of strong, long-range interactions between qubits, but state-of-the-art implementations of entangling gates yield lower fidelities than competing platforms of trapped ions and superconducting systems. Their exists a large gap in fidelities between theoretical proposals and experimental implementations, which can be bridged by technical improvements and pulse shaping. In this work, we propose a procedure for executing a two-qubit controlled phase operation that predicts high fidelity in the presence of decay from excited atomic levels and major technical imperfections. Our results indicate that our gate procedure can pave the way for scalable quantum computing with neutral atoms.

Our procedure for constructing a Rydberg-blockade CZ gate combines our modified TQD technique with the state-of-the-art procedure for implementing CZ gates on atomic qubits [9]. Our symmetric CZ gate is executed between two trapped atoms by simultaneously driving both atoms between their ground and Rydberg levels using focused pulses on individual atoms. We consider both one- and two-photon processes for the ground to Rydberg excitation, which are feasible with current experimental setups [11,57]. Furthermore, we incorporate major sources of technical imperfections in our model, namely Doppler dephasing, atomic-position fluctuation and laser-intensity fluctuation, and make our simulations realistic by using actual values of these imperfections [11]. Our procedure reduces gate errors originating from atom loss and is feasible for implementing CZ gates on large arrays of trapped atoms.

By following our gate procedure, we design time-dependent functions for the Rydberg-excitation lasers that result in high-fidelity CZ gates. These pulse functions are derived from adiabatic pulses by using our modified TQD technique. We analyzed the impact of this technique by comparing pulse shapes and Hamiltonian dynamics. Our results

show that redistributing energy by modifying pulse shapes according to the TQD technique speeds up quantum processes. Additionally, we design a sequence of such modified pulses, with relative phase shifts, to achieve a fast, high-fidelity CZ gate.

We estimate CZ gate fidelities for Cs atom qubits by numerically integrating the quantum master equation. In the presence of spontaneous emission from excited Cs levels and major technical imperfections, our gate procedure deliver CZ gates with fidelities 0.9985 and 0.975 for the one- and two-photon excitation models, respectively. Although one-photon excitation model leads to higher fidelity, its experimental realization is challenging and needs improvements. As compared to adiabatic CZ gates, our gates yield $0.1\times$ the infidelity in $0.15\times$ the gate time requiring $0.3\times$ the pulse energy. The infidelity of the state-of-the-art experimental CZ gate is $2\times$ and the gate time is $3.3\times$ than that of our simulated CZ gate with the same excitation model. Our gates are robust against Doppler dephasing of the Rydberg level and changes in the duration of the Rydberg-excitation pulses Moreover, our gates are less sensitive to thermal fluctuations of atoms and intensity fluctuations of pulses as compared to adiabatic gates.

Our modified TQD technique, which is our key result, can be used to speed up adiabatic dynamics in high-dimensional Hilbert spaces. Although our gate procedure is tailored for Rydberg-blockade gates, our approach of combining TQD with existing gate procedures can be explored for different gates in other quantum computing platforms. Thus our work introduces a powerful pulse-shaping technique in the quantum control toolbox. Similar to the standard TQD technique, our pulse functions are not optimal and their performance efficiencies are limited by the choice of the adiabatic pulses used to derive them. One method to resolve this limitation is by optimal control methods seek superior parameters, perhaps lying outside our chosen parameter domains (56) and (57), for the TQD pulses.

Our results lead to various interesting future directions, and we now present some of them. First, one can apply our modified TQD technique on a two-atom Hamiltonian parametrized by optimized STIRAP pulses [60] to seek higher gate fidelities. Second, adopting a two-photon excitation model for ARP [40,66,67] might be advantageous over STIRAP in terms of gate time and also overcomes the implementation challenges associated with the one-photon ARP model. Third, our modified TQD technique can be used for pulses involved in the above-mentioned two-photon ARP model. Fourth, one can explore techniques, including two-photon ARP, for removing unwanted oscillations in gate fidelity. Finally, one can derive closed-form expressions, similar to Ref. [9], for the two phase-shift parameters in our pulse sequences and exploit the interplay between pulse parameters to improve gate performance.

ACKNOWLEDGMENTS

This project is supported by the Government of Alberta and Natural Sciences and Engineering Research Council of Canada. A.D. acknowledges financial support from Mitacs and computational support from the Digital Research Alliance of Canada.

APPENDIX: MATHEMATICAL PRECEPTS

Here we discuss the decomposition of the 25-dimensional Hamiltonian $\tilde{H}_{\mathrm{B}}^{\mathrm{e}}(t,\boldsymbol{r})$ (41) into a direct sum of one- and two-dimensional Hamiltonians, and the relevant matrix transformations for this decomposition. In this regard, we define an operator that maps the 25-dimensional Hamiltonian to an effective two-dimensional Hamiltonian. The mapping involves matrix transformations which we express as orthogonal matrices for permutation and basis transformation, and idempotent-symmetric matrix for projection. The decomposition and mapping of the time-dependent Hamiltonians are defined at each time t during the dynamics.

1. Transformations

We first define of the transformations and operators that we use in this section. For a Hilbert space $\mathscr{H}$, $\mathcal{B}(\mathscr{H})$ denotes the space of bounded linear operators acting on $\mathscr{H}$. In our case, the transformations, which are basis change and projection, of these operators are represented as conjugating channels. The transformations of the Hamiltonian operators are effected by operators representing the corresponding transformation.

Definition 1. A conjugating-channel transformation is

$$\mathcal{C} : \mathcal{B}(\mathscr{H}) \times \mathcal{B}(\mathscr{H}) \to \mathcal{B}(\mathscr{H}) : (A, B) \mapsto ABA^{\dagger} \tag{A1}$$

for any $A \in \mathcal{B}(\mathscr{H})$, and we use the notation $\mathcal{C}_A(B) = ABA^{\dagger}$. Here A is the transformation operator and B is the Hamiltonian operator.

The decomposition of the Hilbert space $\mathscr{H}$ into two subspaces $\mathscr{H}_1$ and $\mathscr{H}_2$ is represented as a direct sum

$$d = d_1 \oplus d_2, \tag{A2}$$

where d, d_1, and d_2 are the dimensions of $\mathscr{H}$, $\mathscr{H}_1$ and $\mathscr{H}_2$, respectively. A projection on $\mathscr{H}$ is a conjugating-channel transformation (A1), which is executed by a real-valued idempotent operator π with range $\mathscr{H}_1$ and kernel $\mathscr{H}_2$. For the special case of B being a block-diagonal matrix with two blocks $H_1 \in \mathcal{B}(\mathscr{H}_1)$ and $H_2 \in \mathcal{B}(\mathscr{H}_2)$,

$$\mathcal{C}_\pi(B) = \pi B \pi = H_1 \oplus \mathbb{0}_{d_2} =: B', \tag{A3}$$

for $\mathbb{0}_{d_2}$ the $d_2 \times d_2$ null matrix. Thus, the operation π maps a $d \times d$ matrix B to a $d_1 \times d_1$ matrix H_1, padded with a null matrix.

The inverse of a conjugating-channel transformation satisfies

$$\mathcal{C}_A^{-1}(B) = A^{-1}BA^{\dagger^{-1}} = A^{-1}BA^{-1^{\dagger}} \tag{A4}$$

for any invertible A. Particularly, for orthogonal and real-valued A, representing a basis-change operator,

$$\mathcal{C}_A^{-1}(B) = A^{\top}BA. \tag{A5}$$

For a projection operator π satisfying (A3), we define a unique lift operator $\imath$ that executes an inverse projection transformation such that

$$\mathcal{C}_\pi^{-1}(B') = \imath B' \imath \equiv B, \tag{A6}$$

where B and B' are block-diagonal matrices.

2. Decomposition

For our purpose, we first permute the matrix representation of $\tilde{H}^{\rm e}_{\rm B}(t)$ into a block-diagonal structure by the conjugating-channel transformation $\mathcal{C}_{P_1}(\tilde{H}^{\rm e}_{\rm B}(t))$, for a orthogonal and real-valued P_1. This transformation makes $\tilde{H}^{\rm e}_{\rm B}(t)$ a direct sum of 9×9 and 16×16 Hamiltonian matrices, and thus decomposing $\mathscr{H}$ as

$$25 = 5 \otimes 5 \approx 9 \oplus 16. \tag{A7}$$

This block diagonalization is justified by not creating any coupling between levels $\{|0\rangle, |1\rangle, |{\rm r}\rangle\}$, whose tensor products with themselves span the nine-dimensional Hilbert space $\mathscr{H}_{\rm CZ}$, and the other levels $\{|{\rm g}\rangle, |{\rm p}\rangle\}$. In the two-photon case, this decoupling is not strictly true because $|{\rm p}\rangle$ is employed virtually for $|1\rangle \leftrightarrow |{\rm r}\rangle$ coupling, but we eliminate $|{\rm p}\rangle$ by adiabatic methods and thus justify (A7) for the two-photon case.

After a projection transformation $\mathcal{C}_{\pi_1}$ of the block-diagonal Hamiltonian, we obtain a 9×9 Hamiltonian matrix $\tilde{H}^{\rm e}_{\rm B,CZ}(t)$ by

$$\mathcal{C}_{\pi_1} \circ \mathcal{C}_{P_1}\big(\tilde{H}^{\rm e}_{\rm B}(t)\big) = \pi_1 P_1 \tilde{H}^{\rm e}_{\rm B}(t) P_1^{\top} \pi_1 = \tilde{H}^{\rm e}_{\rm B,CZ}(t) \oplus \mathbb{0}_{16}. \tag{A8}$$

This 9×9 matrix represents the unitary dynamics of $\tilde{H}^{\rm e}_{\rm B}(t)$ exactly for the one-photon case and approximately for the two-photon case.

We now perform a permutation transformation $\mathcal{C}_{P_2}$ of $\tilde{H}^{\rm e}_{\rm B,CZ}(t)$ to derive a block-diagonal structure according to the decomposition

$$9 = 3 \otimes 3 = 1 \oplus 2 \oplus 2 \oplus 4 \tag{A9}$$

of $\mathscr{H}_{\rm CZ}$. The singleton arises because there is no coupling between $|00\rangle$ and other levels. The existence of the two-dimensional sectors is justified if only one of the two atoms is in $|1\rangle$ and hence driven by the Rydberg excitation laser to $|{\rm r}\rangle$.

The four-dimensional sector, which represents the case when both atoms are driven, is spanned by a basis set

$$\{|11\rangle, |+\rangle, |{\rm rr}\rangle, |-\rangle\}, \tag{A10}$$

obtained from the standard basis $\{|11\rangle, |1{\rm r}\rangle, |{\rm r}1\rangle, |{\rm rr}\rangle\}$ by transformation $\mathcal{C}_Q$. In this basis the block-diagonal structure (A9) further decomposes as

$$\begin{aligned} 9 =& 1 \oplus 2 \oplus 2 \oplus 4 \approx 1 \oplus 2 \oplus 2 \oplus 2 \oplus 1 \oplus 1 \\ =& \underbrace{\text{span}\{|00\rangle\}}_{\mathscr{H}_0} \oplus \underbrace{\text{span}\{|01\rangle, |0{\rm r}\rangle\}}_{\mathscr{H}_{0{\rm r}}} \oplus \underbrace{\text{span}\{|10\rangle, |{\rm r}0\rangle\}}_{\mathscr{H}_{{\rm r}0}} \\ & \oplus \underbrace{\text{span}\{|11\rangle, |+\rangle\}}_{\mathscr{H}_{\rm rr}} \oplus \text{span}\{|-\rangle\} \oplus \text{span}\{|{\rm rr}\rangle\}. \end{aligned} \tag{A11}$$

where $|-\rangle$ is a dark state and $|{\rm rr}\rangle$ is decoupled from the rest of the states by adiabatic elimination under Rydberg-blockade condition (13).

Finally, we define an effective two-level Hamiltonian $\tilde{H}^{\rm e}_{\rm B,eff}(t)$ as a final projection $\mathcal{C}_{\pi_2}$ of $\tilde{H}^{\rm e}_{\rm B}(t)$ onto $\mathscr{H}_{\rm rr}$. Thus, the whole operation of mapping the 25×25 matrix $\tilde{H}^{\rm e}_{\rm B}(t)$ to a 2×2 matrix $\tilde{H}^{\rm e}_{\rm B,eff}(t)$ is represented by the conjugating-channel transformation

$$\tilde{H}^{\rm e}_{\rm B,eff}(t, \boldsymbol{r}) \oplus \mathbb{0}_{23} = \mathcal{C}_R\big(\tilde{H}^{\rm e}_{\rm B}(t, \boldsymbol{r})\big) \equiv R \tilde{H}^{\rm e}_{\rm B}(t, \boldsymbol{r}) R^{\top}, \tag{A12}$$

for a real-valued operator

$$R := \pi_2 Q P_2 \pi_1 P_1. \tag{A13}$$

$\tilde{H}^{\rm e}_{\rm B,eff}(t)$ drives the transition between $|11\rangle$ and $|+\rangle$ and is primarily responsible for entanglement.

Although the dynamics of the two-atom system can be broken up into independent singleton and qubit evolutions, the initial state $|\psi_0\rangle$ (15) has support over all four Hilbert-space sectors $\mathscr{H}_0$, $\mathscr{H}_{0{\rm r}}$, $\mathscr{H}_{{\rm r}0}$ and $\mathscr{H}_{\rm rr}$. The $|00\rangle$ component of the initial state, i.e., the projection of the initial state onto $\mathscr{H}_0$, undergoes trivial (i.e., identity $\mathbb{1}$) evolution, so the $|00\rangle$ coefficient of the instantaneous state has a constant magnitude during the evolution. As for the other three components of the initial state, their coefficients in the instantaneous state evolve according to the two-level Hamiltonians obtained by projecting $\tilde{H}^{\rm e}_{\rm B}(t)$ onto $\mathscr{H}_{0{\rm r}}$, $\mathscr{H}_{{\rm r}0}$, and $\mathscr{H}_{\rm rr}$, respectively.

[1] M. Saffman, Quantum computing with atomic qubits and Rydberg interactions: Progress and challenges, J. Phys. B **49**, 202001 (2016).

[2] C. S. Adams, J. D. Pritchard, and J. P. Shaffer, Rydberg atom quantum technologies, J. Phys. B **53**, 012002 (2019).

[3] L. Henriet, L. Beguin, A. Signoles, T. Lahaye, A. Browaeys, G.-O. Reymond, and C. Jurczak, Quantum computing with neutral atoms, Quantum **4**, 327 (2020).

[4] M. Morgado and S. Whitlock, Quantum simulation and computing with Rydberg-interacting qubits, AVS Quantum Sci. **3**, 023501 (2021).

[5] X.-F. Shi, Quantum logic and entanglement by neutral Rydberg atoms: Methods and fidelity, Quantum Sci. Technol. **7**, 023002 (2022).

[6] A. Browaeys, D. Barredo, and T. Lahaye, Experimental investigations of dipole–dipole interactions between a few Rydberg atoms, J. Phys. B **49**, 152001 (2016).

[7] D. Jaksch, J. I. Cirac, P. Zoller, S. L. Rolston, R. Côté, and M. D. Lukin, Fast Quantum Gates for Neutral Atoms, Phys. Rev. Lett. **85**, 2208 (2000).

[8] M. D. Lukin, M. Fleischhauer, R. Cote, L. M. Duan, D. Jaksch, J. I. Cirac, and P. Zoller, Dipole Blockade and Quantum Information Processing in Mesoscopic Atomic Ensembles, Phys. Rev. Lett. **87**, 037901 (2001).

[9] H. Levine, A. Keesling, G. Semeghini, A. Omran, T. T. Wang, S. Ebadi, H. Bernien, M. Greiner, V. Vuletić, H. Pichler, and M. D. Lukin, Parallel Implementation of High-Fidelity Multiqubit Gates with Neutral Atoms, Phys. Rev. Lett. **123**, 170503 (2019).

[10] I. S. Madjarov, J. P. Covey, A. L. Shaw, J. Choi, A. Kale, A. Cooper, H. Pichler, V. Schkolnik, J. R. Williams, and M. Endres, High-fidelity entanglement and detection of alkaline-earth Rydberg atoms, Nat. Phys. **16**, 857 (2020).

[11] T. M. Graham, Y. Song, J. Scott, C. Poole, L. Phuttitarn, K. Jooya, P. Eichler, X. Jiang, A. Marra, B. Grinkemeyer *et al.*, Multi-qubit entanglement and algorithms on a neutral-atom quantum computer, Nature (London) **604**, 457 (2022).

[12] M. A. Nielsen and I. L. Chuang, *Quantum Computation and Quantum Information: 10th Anniversary Edition* (Cambridge University Press, Cambridge, 2010).

[13] D. Barredo, S. de Léséleuc, V. Lienhard, T. Lahaye, and A. Browaeys, An atom-by-atom assembler of defect-free arbitrary two-dimensional atomic arrays, Science **354**, 1021 (2016).

[14] M. Endres, H. Bernien, A. Keesling, H. Levine, E. R. Anschuetz, A. Krajenbrink, C. Senko, V. Vuletić, M. Greiner, and M. D. Lukin, Atom-by-atom assembly of defect-free one-dimensional cold atom arrays, Science **354**, 1024 (2016).

[15] T. Xia, M. Lichtman, K. Maller, A. W. Carr, M. J. Piotrowicz, L. Isenhower, and M. Saffman, Randomized Benchmarking of Single-Qubit Gates in a 2D Array of Neutral-Atom Qubits, Phys. Rev. Lett. **114**, 100503 (2015).

[16] Y. Wang, A. Kumar, T.-Y. Wu, and D. S. Weiss, Single-qubit gates based on targeted phase shifts in a 3D neutral atom array, Science **352**, 1562 (2016).

[17] G. Semeghini, H. Levine, A. Keesling, S. Ebadi, T. T. Wang, D. Bluvstein, R. Verresen, H. Pichler, M. Kalinowski, R. Samajdar *et al.*, Probing topological spin liquids on a programmable quantum simulator, Science **374**, 1242 (2021).

[18] S. Ebadi, T. T. Wang, H. Levine, A. Keesling, G. Semeghini, A. Omran, D. Bluvstein, R. Samajdar, H. Pichler, W. W. Ho *et al.*, Quantum phases of matter on a 256-atom programmable quantum simulator, Nature (London) **595**, 227 (2021).

[19] ColdQuanta, https://coldquanta.com/.

[20] QuEra Computing Inc., https://www.quera.com/.

[21] PASQAL, https://pasqal.io/.

[22] Atom Computing, https://atom-computing.com/.

[23] R. Barends, J. Kelly, A. Megrant, A. Veitia, D. Sank, E. Jeffrey, T. C. White, J. Mutus, A. G. Fowler, B. Campbell *et al.*, Superconducting quantum circuits at the surface code threshold for fault tolerance, Nature (London) **508**, 500 (2014).

[24] A. Kandala, K. X. Wei, S. Srinivasan, E. Magesan, S. Carnevale, G. A. Keefe, D. Klaus, O. Dial, and D. C. McKay, Demonstration of a High-Fidelity CNOT Gate for Fixed-Frequency Transmons with Engineered *ZZ* Suppression, Phys. Rev. Lett. **127**, 130501 (2021).

[25] K. Wright, K. M. Beck, S. Debnath, J. M. Amini, Y. Nam, N. Grzesiak, J.-S. Chen, N. C. Pisenti, M. Chmielewski, C. Collins *et al.*, Benchmarking an 11-qubit quantum computer, Nat. Commun. **10**, 5464 (2019).

[26] M. Saffman, I. I. Beterov, A. Dalal, E. J. Páez, and B. C. Sanders, Symmetric Rydberg controlled-*Z* gates with adiabatic pulses, Phys. Rev. A **101**, 062309 (2020).

[27] D. Guéry-Odelin, A. Ruschhaupt, A. Kiely, E. Torrontegui, S. Martínez-Garaot, and J. G. Muga, Shortcuts to adiabaticity: Concepts, methods, and applications, Rev. Mod. Phys. **91**, 045001 (2019).

[28] M. V. Berry, Transitionless quantum driving, J. Phys. A **42**, 365303 (2009).

[29] A. M. Hankin, Y.-Y. Jau, L. P. Parazzoli, C. W. Chou, D. J. Armstrong, A. J. Landahl, and G. W. Biedermann, Two-atom Rydberg blockade using direct 6*s* to *np* excitation, Phys. Rev. A **89**, 033416 (2014).

[30] M. Saffman, T. G. Walker, and K. Mølmer, Quantum information with Rydberg atoms, Rev. Mod. Phys. **82**, 2313 (2010).

[31] T. G. Walker and M. Saffman, Consequences of Zeeman degeneracy for the van der Waals blockade between Rydberg atoms, Phys. Rev. A **77**, 032723 (2008).

[32] T. M. Graham, M. Kwon, B. Grinkemeyer, A. Marra, X. Jiang, M. T. Lichtman, Y. Sun, M. Ebert, and M. Saffman, Rydberg-Mediated Entanglement in a Two-Dimensional Neutral Atom Qubit Array, Phys. Rev. Lett. **123**, 230501 (2019).

[33] I. I. Beterov, D. B. Tretyakov, V. M. Entin, E. A. Yakshina, I. I. Ryabtsev, M. Saffman, and S. Bergamini, Application of adiabatic passage in Rydberg atomic ensembles for quantum information processing, J. Phys. B **53**, 182001 (2020).

[34] W. S. Warren and M. S. Silver, The art of pulse crafting: Applications to magnetic resonance and laser spectroscopy, Adv. Magn. Opt. Reson. **12**, 247 (1988).

[35] J. C. Camparo and R. P. Frueholz, A dressed atom interpretation of adiabatic rapid passage, J. Phys. B **17**, 4169 (1984).

[36] K. Bergmann, H. Theuer, and B. W. Shore, Coherent population transfer among quantum states of atoms and molecules, Rev. Mod. Phys. **70**, 1003 (1998).

[37] V. S. Malinovsky and J. L. Krause, General theory of population transfer by adiabatic rapid passage with intense, chirped laser pulses, Eur. Phys. J. D **14**, 147 (2001).

[38] E. Brion, L. H. Pedersen, and K. Mølmer, Adiabatic elimination in a lambda system, J. Phys. A **40**, 1033 (2007).

[39] I. I. Beterov, M. Saffman, E. A. Yakshina, V. P. Zhukov, D. B. Tretyakov, V. M. Entin, I. I. Ryabtsev, C. W. Mansell, C. MacCormick, S. Bergamini, and M. P. Fedoruk, Quantum gates in mesoscopic atomic ensembles based on adiabatic passage and Rydberg blockade, Phys. Rev. A **88**, 010303(R) (2013).

[40] M. M. Müller, M. Murphy, S. Montangero, T. Calarco, P. Grangier, and A. Browaeys, Implementation of an experimentally feasible controlled-phase gate on two blockaded Rydberg atoms, Phys. Rev. A **89**, 032334 (2014).

[41] Y. Miroshnychenko, A. Gaëtan, C. Evellin, P. Grangier, D. Comparat, P. Pillet, T. Wilk, and A. Browaeys, Coherent excitation of a single atom to a Rydberg state, Phys. Rev. A **82**, 013405 (2010).

[42] X. L. Zhang, A. T. Gill, L. Isenhower, T. G. Walker, and M. Saffman, Fidelity of a Rydberg-blockade quantum gate from simulated quantum process tomography, Phys. Rev. A **85**, 042310 (2012).

[43] S. de Léséleuc, D. Barredo, V. Lienhard, A. Browaeys, and T. Lahaye, Analysis of imperfections in the coherent optical excitation of single atoms to Rydberg states, Phys. Rev. A **97**, 053803 (2018).

[44] M. Saffman, X. L. Zhang, A. T. Gill, L. Isenhower, and T. G. Walker, Rydberg state mediated quantum gates and entanglement of pairs of neutral atoms, J. Phys.: Conf. Ser. **264**, 012023 (2011).

[45] M. Demirplak and S. A. Rice, Adiabatic population transfer with control fields, J. Phys. Chem. A **107**, 9937 (2003).

[46] X. Chen, I. Lizuain, A. Ruschhaupt, D. Guéry-Odelin, and J. G. Muga, Shortcut to Adiabatic Passage in Two- and Three-Level Atoms, Phys. Rev. Lett. **105**, 123003 (2010).

[47] M. G. Bason, M. Viteau, N. Malossi, P. Huillery, E. Arimondo, D. Ciampini, R. Fazio, V. Giovannetti, R. Mannella, and O. Morsch, High-fidelity quantum driving, Nat. Phys. **8**, 147 (2012).

[48] S. Oh, X. Hu, F. Nori, and S. Kais, Singularity of the time-energy uncertainty in adiabatic perturbation and cycloids on a Bloch sphere, Sci. Rep. **6**, 20824 (2016).

[49] Y.-H. Chen, Q.-C. Wu, B.-H. Huang, J. Song, and Y. Xia, Arbitrary quantum state engineering in three-state systems via counterdiabatic driving, Sci. Rep. **6**, 38484 (2016).

[50] J.-L. Wu, X. Ji, and S. Zhang, Fast adiabatic quantum state transfer and entanglement generation between two atoms via dressed states, Sci. Rep. **7**, 46255 (2017).

[51] L.-H. Ma, Y.-H. Kang, Z.-C. Shi, J. Song, and Y. Xia, Shortcuts to adiabatic for implementing controlled-not gate with superconducting quantum interference device qubits, Quantum Inf. Process. **17**, 292 (2018).

[52] T. Wang, Z. Zhang, L. Xiang, Z. Jia, P. Duan, Z. Zong, Z. Sun, Z. Dong, J. Wu, Y. Yin, and G. Guo, Experimental Realization of a Fast Controlled-*Z* Gate via a Shortcut to Adiabaticity, Phys. Rev. Appl. **11**, 034030 (2019).

[53] H. Ribeiro and A. A. Clerk, Accelerated adiabatic quantum gates: Optimizing speed versus robustness, Phys. Rev. A **100**, 032323 (2019).

[54] F. Setiawan, P. Groszkowski, H. Ribeiro, and A. A. Clerk, Analytic design of accelerated adiabatic gates in realistic qubits: General theory and applications to superconducting circuits, PRX Quantum **2**, 030306 (2021).

[55] Y.-X. Du, Z.-T. Liang, Y.-C. Li, X.-X. Yue, Q.-X. Lv, W. Huang, X. Chen, H. Yan, and S.-L. Zhu, Experimental realization of stimulated Raman shortcut-to-adiabatic passage with cold atoms, Nat. Commun. **7**, 12479 (2016).

[56] X. Q. Shao, D. X. Li, Y. Q. Ji, J. H. Wu, and X. X. Yi, Ground-state blockade of Rydberg atoms and application in entanglement generation, Phys. Rev. A **96**, 012328 (2017).

[57] M. J. Martin, Y.-Y. Jau, J. Lee, A. Mitra, I. H. Deutsch, and G. W. Biedermann, A Mølmer-Sørensen gate with Rydberg-dressed atoms, arXiv:2111.14677.

[58] H. Levine, A. Keesling, A. Omran, H. Bernien, S. Schwartz, A. S. Zibrov, M. Endres, M. Greiner, V. Vuletić, and M. D. Lukin, High-Fidelity Control and Entanglement of Rydberg-Atom Qubits, Phys. Rev. Lett. **121**, 123603 (2018).

[59] K. M. Maller, M. T. Lichtman, T. Xia, Y. Sun, M. J. Piotrowicz, A. W. Carr, L. Isenhower, and M. Saffman, Rydberg-blockade controlled-NOT gate and entanglement in a two-dimensional array of neutral-atom qubits, Phys. Rev. A **92**, 022336 (2015).

[60] G. S. Vasilev, A. Kuhn, and N. V. Vitanov, Optimum pulse shapes for stimulated Raman adiabatic passage, Phys. Rev. A **80**, 013417 (2009).

[61] C. A. Sackett, D. Kielpinski, B. E. King, C. Langer, V. Meyer, C. J. Myatt, M. Rowe, Q. A. Turchette, W. M. Itano, D. J. Wineland, and C. Monroe, Experimental entanglement of four particles, Nature (London) **404**, 256 (2000).

[62] R. Storn and K. Price, Differential evolution—A simple and efficient heuristic for global optimization over continuous spaces, J. Global Optim. **11**, 341 (1997).

[63] N. Malossi, M. G. Bason, M. Viteau, E. Arimondo, R. Mannella, O. Morsch, and D. Ciampini, Quantum driving protocols for a two-level system: From generalized Landau-Zener sweeps to transitionless control, Phys. Rev. A **87**, 012116 (2013).

[64] S. Ebadi, A. Keesling, M. Cain, T. T. Wang, H. Levine, D. Bluvstein, G. Semeghini, A. Omran, J.-G. Liu, R. Samajdar *et al.*, Quantum optimization of maximum independent set using Rydberg atom arrays, Science **376**, 1209 (2022).

[65] D. Bluvstein, H. Levine, G. Semeghini, T. T. Wang, S. Ebadi, M. Kalinowski, A. Keesling, N. Maskara, H. Pichler, M. Greiner, V. Vuletić, and M. D. Lukin, A quantum processor based on coherent transport of entangled atom arrays, Nature (London) **604**, 451 (2022).

[66] E. Kuznetsova, G. Liu, and S. A Malinovskaya, Adiabatic rapid passage two-photon excitation of a Rydberg atom, Phys. Scr. **T160**, 014024 (2014).

[67] E. Kuznetsova, Chirped pulse excitation of two-atom Rydberg states, J. Phys. B: At. Mol. Opt. Phys. **48**, 135501 (2015).